The 14th International Topical Meeting on Nuclear Reactor Thermalhydraulics, NURETH-14
Toronto, Ontario, Canada, September 25-30, 2011

NURETH14-027

NUMERICAL SIMULATIONS OF DEVELOPING FLOW AND VORTEX STREET IN A RECTANGULAR CHANNEL WITH A CYLINDRICAL CORE

D. Chang and S. Tavoularis
University of Ottawa, Ontario, Canada

Abstract

Three-dimensional, unsteady simulations of developing turbulent flows in a rectangular channel containing a cylindrical rod have been performed to investigate their sensitivity to the choices of inlet boundary conditions and turbulence models. These effects have been examined by comparing the present predictions with experimental results and with previous predictions using the streamwise-periodic boundary condition. Among all methods, large eddy simulations (LES), employed in a downstream sub-domain of the channel as part of the segregated hybrid model, reproduced most accurately the experimental results. However, the unsteady Reynolds-averaged Navier-Stoke (URANS) simulations are still an acceptable choice for rod bundle analysis, making fairly accurate predictions with a much lower computational cost. Unsteady inviscid (Euler) simulations with a developed inlet velocity distribution predicted the onset of gap instability, which proves that this is an inviscid flow mechanism, associated with the azimuthally inflected velocity distribution. Previous URANS simulations with the streamwise-periodic boundary condition overpredicted the vortex street Strouhal number in rod-bundle flows, whereas the present URANS predictions for a developing flow with uniform inlet velocity were fairly close to the measurements.

1. Introduction

Quasi-periodic flow oscillations across the gap regions of rod-bundle-like channels have been known to exist for more than 50 years [1] and their frequencies and amplitudes for different rod bundle geometries and Reynolds numbers have been measured by many authors (e.g., Hooper and Rehme [2]; Möller [3]; Krauss and Meyer [4]). Guellouz and Tavoularis [5][6], hereafter to be referred as GT, were the first authors to demonstrate conclusively that these flow oscillations are associated with large-scale, vortical coherent structures by employing conditional sampling and phase-averaging to identify and characterize these structures experimentally. More recently, relevant experimental studies have been presented by Baratto et al. [7] for a rod bundle flow and by Lexmond et al. [8], Mahmodd et al. [9] and Khabbouchi et al. [10] for simplified rod-bundle-like channels.

On the computational side, early attempts, based on the solution of the steady, Reynolds-averaged Navier-Stokes (RANS) equations ([11][12][13][14]) failed to simulate accurately flows in rod bundles unless accompanied by heavy use of empirical adjustments ([15][16][17][18][19]). More realistic results were produced by solutions of the Unsteady Reynolds-averaged Navier-Stokes (URANS) equations, first in a preliminary study by Tavoularis et al. [20], but mainly in a series of articles by Chang and Tavoularis [21][22][23][24], hereafter to be referred to as CT. Subsequently, URANS-based simulations of rod-bundle-like flows have been reported by several authors, including Home et al. [25], Ninokata et al. [26] and Yan et al. [27]. Despite the existing ample evidence that RANS simulations are inferior to URANS ones for prediction of flow in narrow gap regions of rod bundles and compound channels, RANS simulations continue to be reported (e.g., Rock et al. [28]; In et al. [29]; Tzanos, [30];

Baglietto and Ninokata, [19]; Házi, [31]; Cheng and Tak, [32]; Cheng and Yu, [33]; Conner, et al. [34]; Liu and Ferng, [35]; Chandra, et al. [36]; Tóth and Aszódi, [37]), A crucial issue when using either RANS or URANS approaches for flows in tightly packed rod bundles is the choice of turbulence model. Yadigaroglu et al. [38] have summarized previous evidence that isotropic turbulence models based on the Boussinesq eddy-viscosity approximation are not adequate to predict turbulent rod bundle flows. Nevertheless, the isotropic turbulence models remain in use by some researchers (e.g., Home et al. [25]; Conner, et al. [34]), because of their relative stability and lower computational time compared to anisotropic turbulence models like Reynolds stress models (RSM). Unlike URANS, numerical studies using large-eddy simulations (LES) or direct numerical simulations (DNS) are mostly limited to flows at relatively low Reynolds numbers, because of their excessive requirements in terms of computational mesh density and running time. Even so, LES simulations of flows in rod bundles and other compound channels have been undertaken by several authors, including Mayer and Házi [39], Mayer et al. [40], Wang and Pletcher [41], Merzari et al. [42], Abbasian et al. [43][44], and Ikeno and Kajishima [45], whereas DNS studies include those by Baglietto et al. [46], Mayer and Házi [39], and Ninokata et al. [26].

One issue of concern in some of the previous numerical studies of rod bundle flows has been the use of the streamwise-periodic boundary condition [21][22][23][24][26][27][37][39][40][42][44][45][46]. When applied to relatively short channels, such boundary conditions may introduce disconcerting numerical artefacts, but, even if applied properly, would strictly correspond to flows in infinitely long channels, a condition that does not apply to practical systems. For example, the typical 37-rod bundle of the CANDU (CANada Deuterium-Uranium) nuclear reactor, which is a type of pressurized heavy water reactor (PHWR) has a length that is equal to approximately 64 hydraulic diameters or 38 fuel element diameters. Thus, in a large section of the bundle, if not in its entirety, the flow would be developing, even in the absence of endplates, spacers and other obstructions. A number of concerns that apply to both simulations and experiments in rod bundle flows have been raised by Tavoularis [47], who has also suggested a nomenclature for large scale motions in rod bundles. According to this nomenclature, the coherent motions across a single rod gap are termed as "gap vortex street," whereas all coherent motions in a rod bundle are collectively termed as "rod bundle vortex network;" the flow instability that leads to the generation of a gap vortex street is termed as "gap instability."

The objective of this study is to simulate developing turbulent flow in a rod-bundle-like channel for which detailed measurements, including measurements in a narrow gap region, are available. In view of the GT measurements, which can be used for validation of the simulations, and the previous CT simulations, which may be used for comparisons, we decided to use the GT/CT geometry, which consists of a rectangular duct containing a cylindrical rod. Although this configuration is simpler than rod bundles used in conventional nuclear reactors, it has two essential elements in common with practical rod bundles: first and foremost, the narrow gap region between a cylindrical rod and a pressure vessel wall, which is the necessary condition for the formation of a gap vortex street; and second, corner sections, similar to those present in square-pitched fuel rod bundles in pressurized water reactors (PWR). The wall-gap to rod-diameter ratio for the GT/CT configuration is 1.10, somewhat lower than the value of 1.149 for a typical CANDU 37-rod bundle.

The present analysis aims at investigating in depth the main issues that have been identified in previous numerical simulations of flows in rod bundles and related geometries. Several different numerical approaches were tested. The reported results correspond to a) URANS predictions of developing flow with a uniform inlet velocity; b) URANS predictions of developed flow in an essentially infinitely long duct, achieved by using the streamwise-periodic boundary condition; c) URANS simulations

addressing the effect of inlet turbulent intensity; d) comparison of URANS predictions with RANS predictions; e) URANS predictions with an inlet velocity distribution that matches the time-averaged mean velocity distribution in an infinite duct. In addition, we report results of unsteady simulations of developing flow using different turbulence models. These include URANS with RSM-ε (Reynolds stress model by Launder and Shima) and RSM-ω (Reynolds stress model by Wilcox), scale-adaptive simulations (SAS), improved delayed detached eddy simulations (IDDES), and segregated (or zonal) hybrid simulations. The results of these simulations have been compared to each other and to experimental results.

In addition to the unsteady viscous flow simulations, we also conducted unsteady inviscid (Euler) simulations for the following reason. Gosset and Tavoularis [48] and Piot and Tavoularis ([49], in press) have explained the formation of the gap vortex street as the result of the instability of the two azimuthal shear layers that form on either side of the gap, following a mechanism that is related to the well known Kelvin-Helmholz (KH) instability process. Previous authors have demonstrated that vortices are generated near the gap centre and then their mutual interactions organize them into a vortex street, reminiscent of the von Kármán vortex street. As the KH instability is an inviscid process, it would be interesting to explore the hypothesis that a gap vortex street can appear in an inviscid flow through a channel that has a narrow gap. Of course, if one performs an inviscid (Euler) simulation in a channel with a uniform inlet velocity, nothing is going to happen, as the velocity in the entire channel will remain uniform throughout time. To test the previous hypothesis, one needs to start the unsteady Euler calculations from an inlet condition that imposes azimuthal shear layers with azimuthal profiles of the axial velocity that have inflection points. A suitable inlet condition is a velocity distribution that matches the fully-developed, time-averaged velocity distribution in the present channel. The outcome of this analysis is expected to contribute to the understanding of gap instability.

2. Computational procedures

2.1 Computational geometry and flow conditions

The geometry and conditions used in the present study were meant to reproduce the ones in the experiments by GT, namely isothermal flow in a rectangular channel containing a cylindrical rod, as shown in Fig. 1. The origin of the Cartesian coordinate system is located in the middle of the bottom wall of the inlet plane, with the axes x, y and z, respectively, pointing toward the streamwise, transverse (normal to the bottom wall) and spanwise directions. The inner dimensions of the rectangular channel were 2.0D (height), 3.0D (width) and 54.0D (length), with D representing the rod diameter. Only measurements on a cross-section 1.8D upstream of the channel outlet have been reported and, although some qualitative evidence indicated that coherent structures were present far upstream of the exit, no attempt was made to characterize the flow in the entire channel, neither to document the inlet conditions. The gap between the rod and the adjacent bottom wall was 0.10D and the Reynolds number, based on the bulk velocity U_b and the hydraulic diameter $D_h = 1.59D$, was 108,000.

In the present simulations, the cross-section dimensions were identical to those in the experiments, whereas the computational domain length was set to $L = 108D$ for all cases except the segregated hybrid simulations. Although it was preferable to keep the same length as the one of the GT experiment, it was decided to double the length, in order for the flow to approach full development at the channel's exit. For the segregated hybrid simulations, the domain was decomposed into two sub-domains: an upstream domain ($0 \le x/D \le 45$), in which SAS were conducted, and a downstream domain ($45 < x/D \le 65.8$), where LES was used. The relatively short length of the downstream domain was dictated by the requirements of LES.

The inlet flow conditions for the URANS simulations were a uniform or a non-uniform velocity distribution, and a turbulence intensity of either 3% or 10%. The use of uniform turbulence intensity at the inlet is justifiable in view of the wide scale separation between the large-scale vortices and the small-scale turbulence [50]. However, for the SAS, the IDDES and the segregated hybrid model simulations, time-varying velocity fluctuations need to be specified at the inlet. The SAS and IDDES employed the spectral synthesis method (SSM), whereas the segregated hybrid model simulation used the synthetic eddy method (SEM). The SSM, developed by Kraichnan [51] and modified by Smirnov et al. [52], employs the summation of Fourier harmonics with random coefficients to generate a velocity fluctuation field. The velocity fluctuation field is later modified using the correlation tensor and information on the length and time-scales of the turbulence from other experiments and simulations. The SEM, proposed by Sergent [53], adopts the particle discretization method to solve the 2D vorticity distribution on the inlet plane for the lateral components of the velocity fluctuation. Then it employs the linear kinematic model [54] to get the streamwise velocity fluctuation. A uniform static pressure was specified at the outlet for all simulations except for the segregated hybrid model simulations; the latter used the outflow boundary condition, which extrapolates the data inside the computational domain by assuming a zero diffusion flux at the outlet.

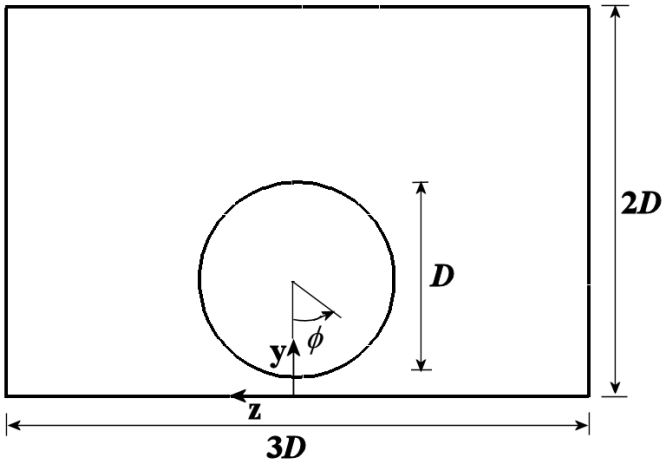

Figure 1. Sketch of the computational cross-section and definition of coordinates and dimensions.

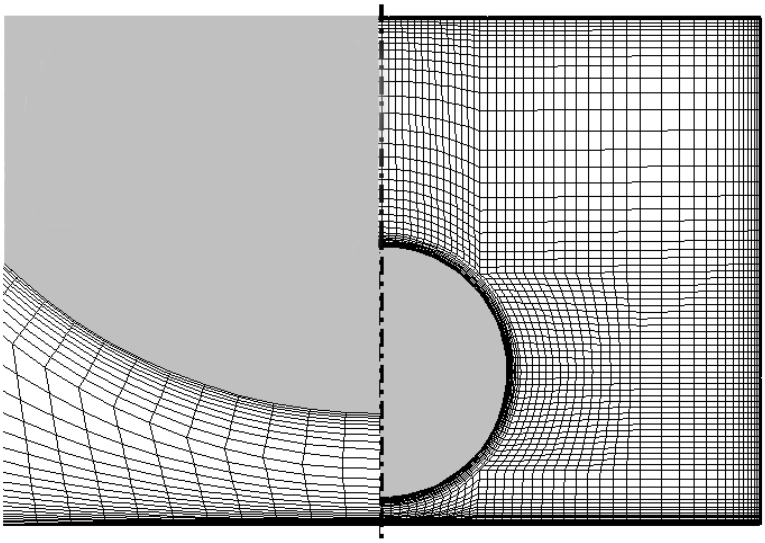

Figure 2. The computational mesh of the cross-section (right), with a detail in the gap region (left).

2.2 Numerical methodology

For all present simulations, the channel cross-section was mapped using a multi-block, structured grid, with 77×90 hexahedral elements (Fig. 2); the streamwise length of each element was $\Delta x = 0.251D$, which corresponds to 431 grid points over the length of the channel. Thus, the total number of elements was approximately 3 million. For the mesh dependence study, a finer mesh, comprising approximately 6 million elements, was generated by allocating 862 streamwise grid points, such that each element had a length equal to $\Delta x = 0.126D$, while keeping an identical mesh distribution on the cross-section. URANS with RSM-ε and a uniform inlet velocity were used for the mesh dependence study. For an evaluation of the mesh size effect, the time-averaged axial velocities in the gap centre at $x = 50D$ and $100D$ were calculated for the two meshes. The differences for two meshes were 0.3% and 1.9%, respectively. In order to avoid the excessive computational time required by the finer mesh, we adopted the coarser of the two meshes as the standard. This choice does not apply to the segregated hybrid simulations, because they required a high-density mesh for the LES zone. For these simulations, 431 streamwise grid points were used in the downstream domain, which has a length of $10.8D$, so that 3 million elements, each with a length $\Delta x = 0.003D$, were located in the LES domain. For the SAS

domain, 431 streamwise grid points were allocated over the length of 45.0D, so that each element had a length $\Delta x = 0.104D$ and the number of elements in the SAS domain was also about 3 million. Therefore, the total number of elements for the segregated hybrid simulation was about 6 million. The adequacy of the mesh resolution for the LES was determined by satisfying the criteria discussed by Georgiadis et al. [55], namely $50 \le \Delta x^+ \le 150$, $\Delta y^+_{\text{wall}} \le 1$ for the top and bottom walls and $\Delta z^+_{\text{wall}} \le 1$ for two side walls. In these expressions, $\Delta x^+ = \rho \Delta x u_\tau / \mu$ is the dimensionless streamwise grid spacing; ρ is the density; Δx is the streamwise grid spacing; $u_\tau = \sqrt{\tau_{\text{w}} / \rho}$ is the friction velocity; τ_{w} is the wall shear stress; μ is the dynamic viscosity; $\Delta y^+_{\text{w}} = \rho \Delta y_{\text{w}} u_\tau / \mu$ is the dimensionless transverse grid spacing normal to the wall (Δy_{w} is the transverse spacing between the first grid point and the top or bottom wall); $\Delta z^+_{\text{w}} = \rho \Delta z_{\text{w}} u_\tau / \mu$ is the dimensionless spanwise grid spacing (Δz_{w} is the spanwise spacing between the first grid point and one of the side walls). For the LES zone, it was estimated that $\Delta x^+ \approx 53.9$ and $\Delta y^+_{\text{w}} \approx \Delta z^+_{\text{w}} \approx 1.2$. The stretching ratio between two consecutive grid points as they moved away from the wall was 1.2 in both the transverse and the spanwise directions. It was thus determined that the mesh for the LES was fine enough to resolve the turbulence scales in the near-wall region, as it was close to satisfying the grid spacing criteria. The time step size Δt was also deemed to be sufficiently small, as the CFL (Courant-Friedrichs-Lewy) number $U_{\text{b}} \Delta t / \Delta x$ was equal to 0.15 for all cases except for the segregated hybrid model. Reduction of the grid element sizes for the segregated hybrid model led to increases of the CFL number to 0.36 and 12.54 for the SAS and the LES zones, respectively. Although the CFL number for the LES was relatively high compared to usual LES practice, we were forced to accept it in order to avoid having excessive computing time; it is noted that each current LES simulation required approximately three months of running time in a Dell cluster consisting of 6 Power Edge SC servers, each with 2 × Quad core, 2.0 GHz AMD Opteron processors, for a total of 40 threads.

The development of the flow patterns was checked by monitoring the fluctuations of the spanwise velocity in the gap center, which are known to be sensitive indicators of coherent vortical structure effects. For the URANS with RSM, a steady-state of such patterns was achieved following a computational time equal to 4.2t, where $t = L / U_{\text{b}}$ is the average flow turn-over time, namely the average time that it takes for the fluid to pass through the computational domain. The transient time for arriving at the steady state was 12.6t for the segregated hybrid model simulations. Following steady-state attainment, for most simulations (excluding those with the segregated hybrid model simulations), flow parameters were collected for statistical processing over 0.9t, which corresponds to 2510 time steps (17 days of computing), or approximately 18 cycles of spanwise velocity fluctuations. For the segregated hybrid model simulations, the collecting time was 2970 time steps (90 days of computing), which corresponds to the 19.7 cycles of spanwise velocity fluctuations.

All simulations have been conducted using the commercial package FLUENT, versions 6, 12 and 13. All URANS simulations and the unsteady Euler simulations employed the second-order upwind scheme for the convection terms of the transport equations, whereas SAS, IDDES, and the segregated hybrid simulations used the bounded central-difference scheme. The pressure is interpolated at the cell faces using the Rhie-Chow scheme [56] to avoid pressure oscillations (checker-boarding) under the constraint of mass conservation. The second-order implicit Euler scheme was employed for temporal discretization. To avoid numerical instability caused by the combination of high-aspect ratio grid cells and highly-clustered near-wall spacing, as required for turbulence modelling, the SIMPLEC (Semi-

Implicit Pressure Linked Equations – Consistent) algorithm was used for the treatment of pressure-velocity coupling [57].

2.3 Turbulence models

The present simulations include URANS with two kinds of Reynolds stress models (RSM), one suggested by Launder and Shima (RSM-ε) and another suggested by Wilcox (RSM-ω), Scale Adapted Simulations (SAS), which are second generation URANS, as well as hybrid simulations of two kinds, namely Improved Delayed Detached Eddy Simulations (IDDES) and segregated hybrid model simulations.

The RSM determine the turbulent stresses by solving a transport equation for each stress, without using the Boussinesq eddy-viscosity approximation. For the present geometry, RSM are preferable over one- and two-equation models, because only RSM can resolve the strong turbulence anisotropy in the gap region as well as the secondary flows in the corners of the channel. Unlike one- and two-equation models, RSM account for the effect of flow history by using terms representing the convection and diffusion of the stress tensor. For the RSM-ε, the pressure-strain rate tensor is modeled using a low-Reynolds version of the linear pressure-strain model with coefficient values as suggested by Launder [58] and Launder and Shima [59]; this model has a slow pressure-strain term, a fast pressure-strain term and a wall reflection term. Because of the wall reflection term, the near-wall region should be treated separately; the two available approaches are the use of a wall function and the two-layer model. It was deduced that the wall function approach would not be suitable for the domain near a narrow gap, which would be subjected to strong cross flows. Thus, the two-layer wall model was adopted, for which the computational domain was divided into the near-wall region and the turbulent core flow region, depending on the Reynolds number based on wall distance. To bridge smoothly the turbulent viscosity and dissipation in the near-wall region to the corresponding values in turbulent core flow, the turbulent viscosity was computed from an one-equation model (viscous damping function), which avoids the inconsistency of the dissipation rate equation in the near-wall layer [60]. The RSM-ω uses a simplified version of the Launder-Reece-Rodi model [61] to model the pressure-strain rate term and the specific dissipation rate (ω) equation to close the stress transport equations [62]. This model does not need a viscous damping function to resolve flows near walls.

The SAS introduces source terms in the ω equation in terms of the von Kármán length scale, which is the ratio of the first and the second velocity gradients. The SAS acts as the LES in unsteady regions where the von Kármán length scale is reduced, while it works as the URANS in the steady regions where the von Kármán length scale is increased. In this work the shear stress transport (SST) model was chosen as the turbulence model for the URANS. The SAS model can resolve scales without grid information as it contains no explicit term specifying the grid spacing. Details have been provided by Mentor and Egorov [63].

Before proceeding with the use of hybrid models, we investigated whether the LES resolving the wall region could be performed for the present flow, in which Re = 108,000. According to Chapman [64], the number of mesh cells required to resolve the inner wall layer would be proportional to $Re^{1.8}$, which implies that the present simulations would require a mesh with a number of elements of the order of 10^9, which far exceeds the available computational resources. Therefore, the only possible approach to introduce LES is to perform hybrid simulations.

The detached eddy simulation (DES) was proposed by Spalart et al. [65]. It employs a RANS model in the near-wall region and an LES model in the turbulent core flow. The DES has been used mostly for external flows with highly separated regions, for which the capabilities of turbulence models are known to deteriorate. In recent years, the DES has also been used in wall bounded flows at high Reynolds numbers, as an alternative to the LES due to its lower computational requirements. In such cases, however, the LES model could be activated in the near-wall region when the grid limiter, which distinguishes the regions for the LES and the RANS, is smaller than the boundary layer thickness. To resolve this grid limiter problem, Shur et al. [66] introduced the improved delayed detached eddy simulation (IDDES), which has a grid limiter formulation that preserves the RANS mode in the near-wall region. In the present study, the RANS with the SST model was used in the near-wall region and it was switched to the LES in the region where the turbulent length scale predicted by the RANS is larger than the local grid spacing. In the SST model, the destruction term depends on the turbulent length scale. Thus, this model is less sensitive to grid resolution than the DES.

The segregated hybrid model simulation by Mathey [67] divides the computational domain into sub-domains and allows one to assign different turbulence models to each sub-domain. In the present analysis, the SAS was assigned to an upstream, relatively long sub-domain, whereas the LES was assigned to a downstream, relatively short sub-domain. In the interface between the SAS and the LES, the velocity fluctuation was modeled by using the SEM [53]. The wall-adapting local eddy-viscosity (WALE) model [68] was chosen as a subgrid model for the LES because this subgrid model is capable of predicting correctly the asymptotic flow behaviour near the wall in wall-bounded turbulent flows, due to its use of the square of the velocity gradient tensor (refer to recent journal articles [69][70][71]).

A summary of the conditions for all developing turbulent flow simulations conducted in this study is given in Table 1.

Table 1. Summary of numerical specifications for developing flow simulations

Developing flow simulations		inlet velocity distribution		inlet turbulent intensity (%)	time-varying velocity algorithm	outlet condition	domain length	convection scheme
		uniform	fully developed					
URANS with RSM-ε		√		3.0		pressure	108*D*	second-order upwind
URANS with RSM-ε		√		10.0		pressure	108*D*	second-order upwind
RANS with RSM-ε		√		3.0		pressure	108*D*	second-order upwind
RANS with k-ε		√		3.0		pressure	108*D*	second-order upwind
URANS with RSM-ε			√	3.0		pressure	108*D*	second-order upwind
URANS with RSM-ω		√		3.0		pressure	108*D*	second-order upwind
SAS		√		3.0	SSM	pressure	108*D*	bounded central-difference
IDDES		√		3.0	SSM	pressure	108*D*	bounded central-difference
segregated hybrid	SAS (up-stream)	√		3.0	SEM	interface	45*D*	bounded central-difference
	LES (down-stream)	interface			SEM	outflow	11*D*	bounded central-difference
Euler			√			pressure	108*D*	second-order upwind

2.4 Identification of vortex streets

Vortex streets are repeating patterns of coherent vortical structures. The identification of coherent vortical structures in the present study was based on the modified Q criterion, defined as

$$Q_{\mathrm{m}} = \frac{1}{2}\left(\Omega_{ij}\Omega_{ij} - c_{\mathrm{q}}\, S_{ij}S_{ij}\right) \tag{1}$$

where $c_{\mathrm{q}} > 1.0$ is an empirical factor which amplifies the effect of the rate of strain tensor S_{ij} relative to the effect of the rate of rotation tensor Ω_{ij}. By selecting c_{q} = 1.2 and a threshold of 1 s^{-2}, it became possible to identify the surfaces of realistic coherent vortical structures. It is noted that the use

of the conventional Q criterion, for which $c_q = 1.0$, failed to identify the gap vortices in a consistent manner.

In order to compare the results of the URANS computations with time-averaged measurements, one needs to consider both coherent and non-coherent time-averaged contributions, computed over a time interval that is sufficiently long to capture a significant number of coherent vortical structures. The kinetic energy of the coherent velocity fluctuations is obtained by time averaging the sum of the squares of the resolved velocity fluctuations, whereas the non-coherent turbulent kinetic energy is obtained by time averaging the sum of the normal Reynolds stresses provided by the solutions of the Reynolds stress equations. The total time-averaged turbulent kinetic energy per unit mass is determined as the sum of the coherent and non-coherent turbulent kinetic energy terms [21].

3. Results

3.1 Comparison of streamwise-periodic and developing flow simulations using URANS and the RSM-ε

New simulations have been conducted for developing flow in a duct with a length of 108D using the URANS with the RSM-ε and a uniform inlet velocity. The objective of these simulations was to permit comparisons with the CT study, which used the same numerical method to simulate flow in a duct with a length of 20D, while also enforcing the streamwise-periodic boundary condition, thus generating results corresponding to a duct with essentially infinite length.

Figure 3 shows a typical instantaneous streamwise profile of the cross-stream velocity along the centreline of the gap. In this particular profile, no cross-flow oscillations are visible for $x/D < 37$; in the range $37 < x/D < 50$, strong oscillations built up rapidly; the amplitude of these oscillations reached a mild peak at $x/D = 50$, and for $57 < x/D$ it settled at a value of roughly $0.18U_b$. This is clear evidence for the onset of gap instability and the formation of a gap vortex street at some intermediate location within the channel. The wavelength between consecutive peaks of the spanwise velocity fluctuated from one cycle to the next, but it was clear that it generally increased toward the outlet (Fig. 3b). The average wavelength over 9 cycles in the range $60 < x/D < 98$ was 4.2D; this value matched the experimental value of about 4.2D but it was lower than the CT prediction of 4.9D. The standard deviation of local temporal fluctuations of the cross-flow velocity is also shown in Fig. 3; as was the case for the velocity amplitude, this parameter reached a mild peak of $0.13U_b$ at $x/D = 52$, and for $60 < x/D$ it settled at a value of roughly $0.12U_b$. This demonstrates that the instantaneous velocity profile shown in Fig. 3 is representative of the overall flow pattern.

Figure 4 shows a snapshot of the gap vortex street and the streamlines on the equidistant plane, namely a plane parallel to the bottom wall and half way between the wall and the rod. The modified Q criterion captured clearly the locations and sizes of the gap vortex street. To indicate its rotational direction, each vortex was coloured by the transverse (normal to the bottom wall) component of vorticity ω_y, normalized by U_b / D_h. Figure 4a shows a front view of the vortex street, as well as the rod cross-section, the bottom wall and the equidistant plane. It is clear in Fig. 4a that all vortices were located on either side of the rod. Their sizes increased gradually along the main flow direction, as shown in the side view, Fig. 4b. The heights of the identified parts of the vortices reached up to 1.2D and their widths reached 0.8D, which shows that these vortices extended over a considerable part of the channel cross-section. Figure 4c is a top view of the vortex street and shows quasi-streamlines on the

equidistant plane. Small vortices first appeared near the middle of the gap at $x/D \approx 37$, where the cross-flows started to develop (Fig. 3); further downstream, these vortices increased in size, while their axes shifted sideways to $z/D \approx \pm 0.52$ from the middle of the gap. For $42.2 \le x/D$, contours of transverse vorticity indicated that vortices rotated clockwise for $0 < z/D$ and counter-clockwise for $z/D \le 0$. Figure 4d is similar to Fig. 4c, except that, in the former, the quasi-streamlines correspond to a frame convected with the speed of the vortices (see later discussion) and demonstrate that the vortices located in each side of the gap transported fluid across the gap and into the opposite open sub-channel. The presence of a secondary vortex street (marked by ellipses) may also be seen in Fig. 4, These vortices seem to correspond to weak flow oscillations in the wide gap between the rod and the top wall.

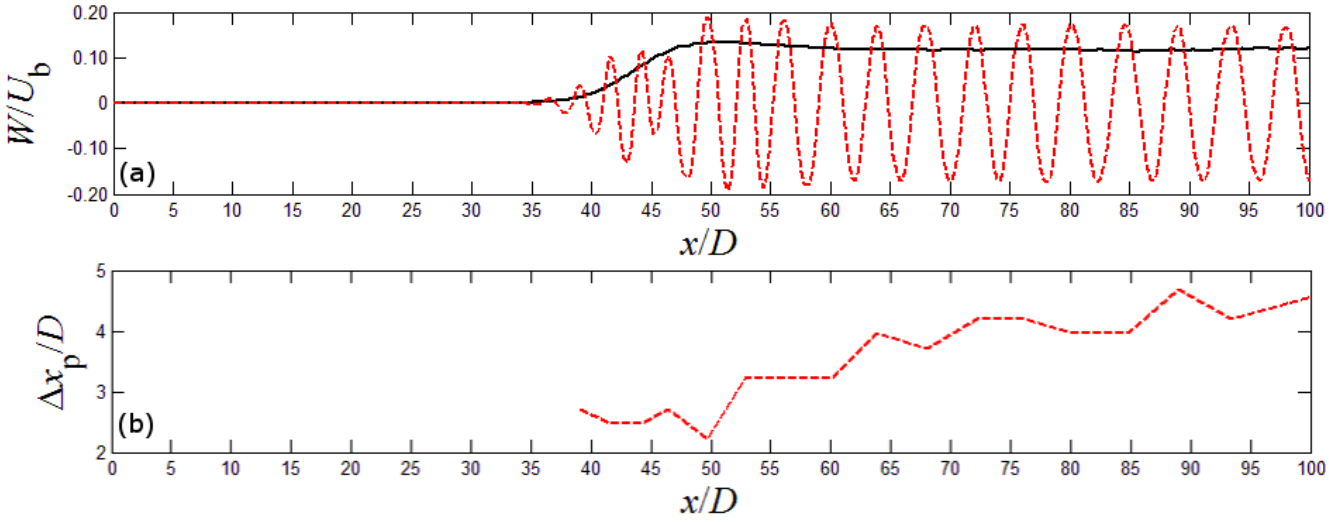

Figure 3. (a) A typical instantaneous streamwise profile of the cross-flow velocity along the gap centreline (– –) and the standard deviation of local cross-flow fluctuations (——); (b) normalized distance $\Delta x_p / D$ between two consequent positive peaks of the instantaneous profile of the cross-flow velocity.

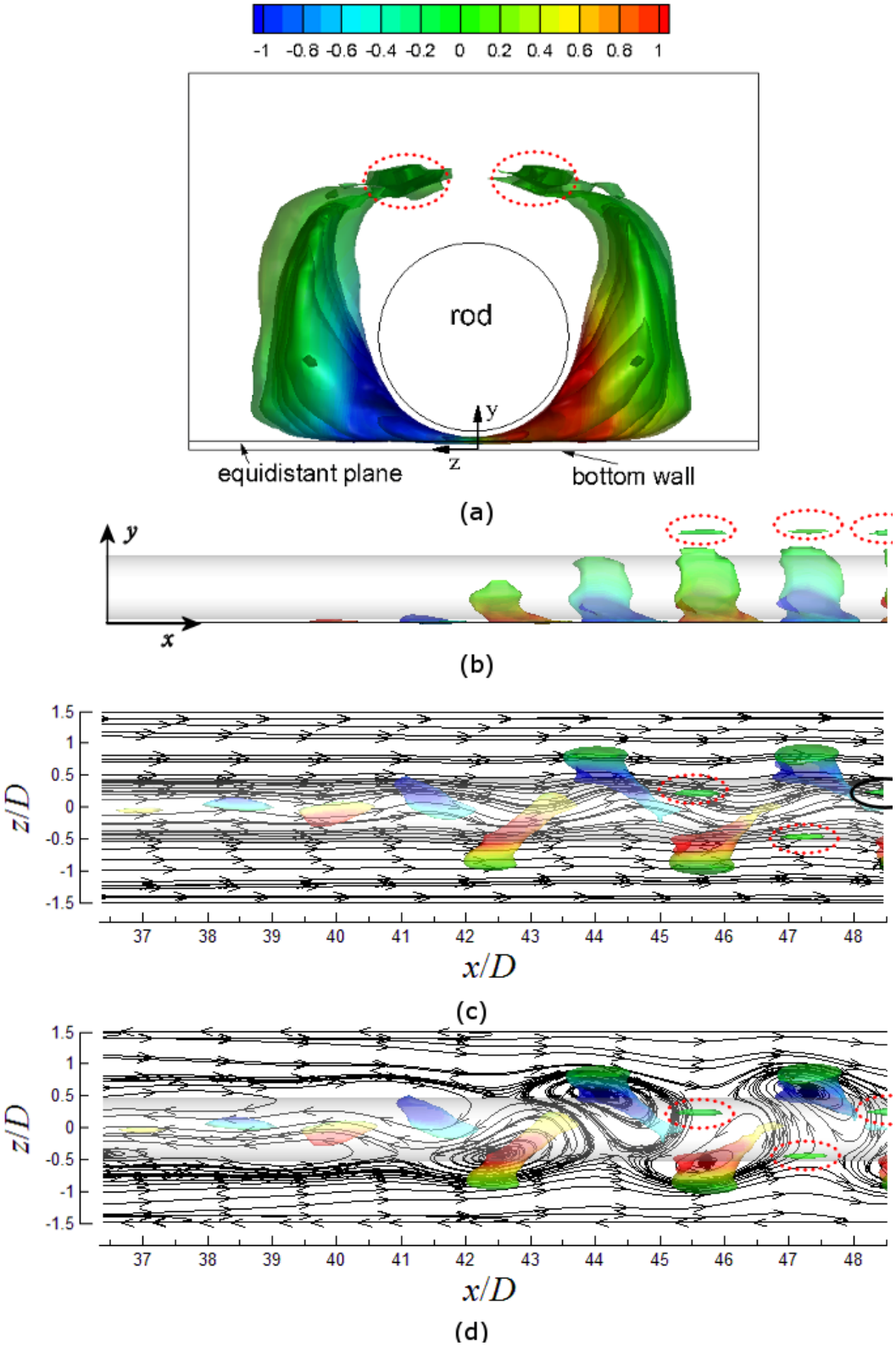

Figure 4. Gap vortex street identified by the modified Q criterion; (a) front view of the rod and the gap vortex street, coloured by the normalized traverse vorticity component $\omega_y D_h / U_b$; (b) side view of the gap vortex street; (c) gap vortex street and quasi-streamlines on the equidistant plane in the absolute reference frame; (d) same as (c), but in a frame moving with the convective speed of the gap vortex street; ellipses mark secondary vortices.

Figure 5 shows contours of the velocity components, normalized by the bulk velocity, superimposed on corresponding cross-sections of the gap vortex street. The spanwise velocity contours in Fig. 5a had their peaks in the middle of the gap and reached values up to ± 0.2. Subsequent peaks had opposite values, which is consistent with the cross-flow velocity profile in Fig. 3. The transverse velocity contours in Fig. 5b reached positive peaks of 0.020 at $z/D \approx \pm 0.19$ and negative peaks of –0.016 at $z/D \approx \pm 0.18$ (the slight asymmetry is not disconcerting, as these are instantaneous contours). These peaks were located at the same axial positions as the spanwise velocity peaks. The spanwise location of the transverse velocity peaks is likely particular to the geometry of this channel and one should not apply it to rod bundle flows. The axial velocity contours in Fig. 5c show a similar pattern as the streamlines in Fig. 4c. It is worth noting that, in the middle of the gap, the local axial velocity at $x/D > 48.5$ was much higher (by $0.3U_b$) than the corresponding value at $x/D = 36$, i.e., upstream of the gap vortex street start. This clearly demonstrates that the formation of the gap vortex street not only created cross-flows across the gap, but also raised markedly the axial velocity in the gap region, thus enhancing the local convective heat transfer.

To characterize the flow oscillations across the gap, the power spectral density of the cross-flow velocity in the centre of the gap was obtained using Matlab with the Burg algorithm. Figure 6 shows the smoothened power spectral density at two different streamwise positions (x/D = 50 and 100), plotted vs. the dimensionless frequency $f D/U_b$ where f is the frequency. Each of the spectra has a distinct main peak at a frequency f_p, which defines the Strouhal number of the gap vortex street as

$$\mathrm{St} = \frac{f_p D}{U_b} \tag{2}$$

At x/D = 50, St = 0.20, which is 18% higher than the experimental value [5] of 0.17 but lower than the CT prediction of 0.27 [21]. At x/D = 100, St = 0.17, which agrees with the experimental value. These observations indicate that the CT overestimation of the Strouhal number was not caused by some inadequacy of the URANS method, neither by flow development considerations, but is likely an artefact of the imposition of the streamwise-periodic boundary condition over a relatively short channel domain. This conjecture is supported by the fact that Chang and Tavoularis [23], who performed URANS simulations with RSM and the streamwise-periodic boundary condition for a turbulent flow in a 37-rod bundle, also predicted a gap vortex street Strouhal number that was roughly twice the experimental value of Baratto et al. [7], even though their predictions of the time-averaged mean velocity and turbulence characteristics were in good agreement with experimental results by Ouma and Tavoularis [72][73].

Figure 7 shows comparisons of the present predictions of the time-averaged axial velocity with the GT [5] experiments and the CT simulations [21]. Although the CT simulations reproduced quite well the bulging of the experimental velocity contours in the gap region and in the corners of the channel, they had a notable difference from the GT experiments in the maximum velocity location. CT predicted a maximum velocity on the symmetry plane above the rod (Fig. 7b), whereas GT found the maximum velocity to be in the open channel, half way between the symmetry plane and the side wall (Fig. 7a). In the present developing flow simulations, the location of the maximum velocity changed downstream: at x/D = 50 (Fig. 7c), it was in the open channel, comparable to the experimental finding (Fig. 7a); at $x/D = 100$ (Fig. 7d), however, it shifted toward the symmetry plane above the rod, indicating that at even higher x/D it might approach the CT predictions (Fig. 7b), which correspond to an infinitely long channel. The values of the contours in all cases differed by a very small percentage, if at all.

Considering differences between the experimental and computational geometries, the lack of exact specifications for inlet conditions, and the uncertainties inherent to both simulations and experiments, one may confidently conclude that, at least as far as the overall mean velocity distribution is concerned, the agreement between the present simulations and the GT experiments is fairly good.

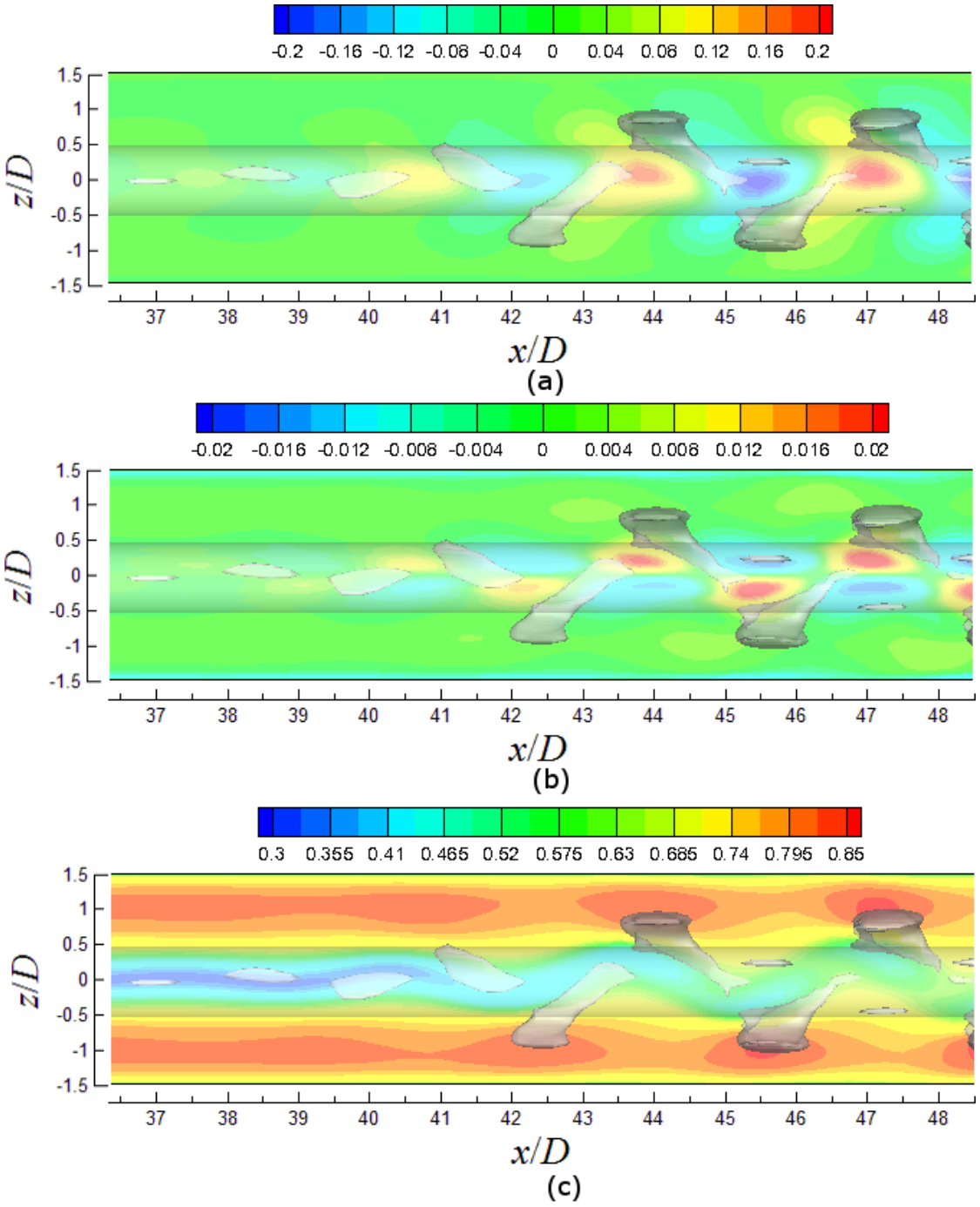

Figure 5. Instantaneous top views of the gap vortex street and isocontours of the normalized velocity components on the equidistant plane: (a) spanwise velocity W/U_b, (b) transverse velocity V/U_b, and (c) axial velocity U/U_b.

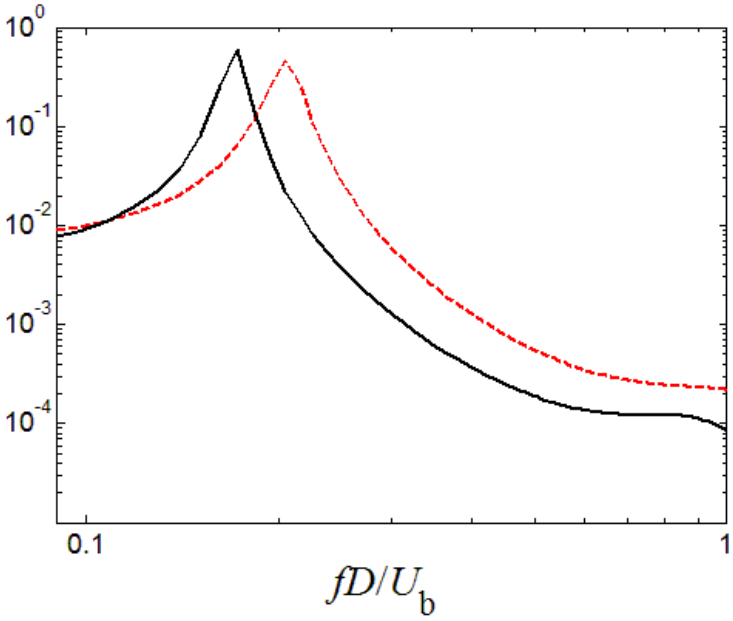

Figure 6. Power spectral density of the spanwise velocity fluctuation in the centre of the gap at x/D = 50 (– –) and 100 (——).

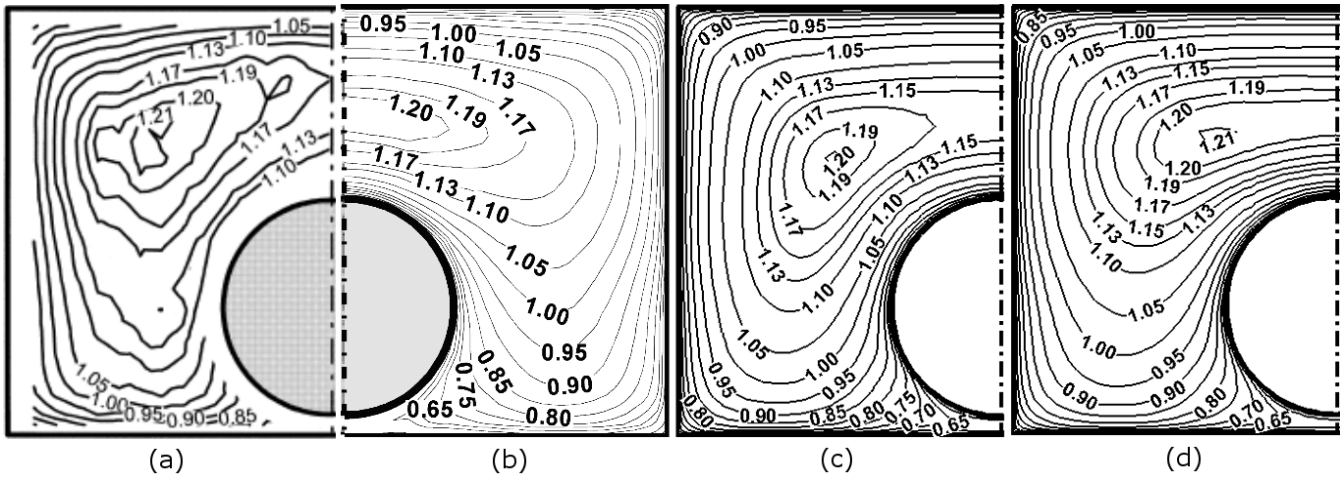

Figure 7. Isocontours of the time-averaged dimensionless axial velocity U/U_b: (a) GT experiments; (b) CT simulations; (c) present URANS simulations with RSM-ε and uniform inlet velocity at x/D = 50; (d) same as (c) but at x/D = 100.

Figure 8 shows detail views of the local time-averaged dimensionless streamwise velocity in the gap region and compares isocontours obtained by GT (Fig. 8a) and CT (Fig. 8b) with those at x/D = 50 and 100 from the present simulations. The present simulations have better agreement with the GT measurement data than the CT simulations. The present local velocity predictions decreased downstream away from the gap, but they were nearly insensitive to the streamwise position in the gap region (Figs 8c and 8d). The distribution of axial velocity at x/D = 100 was closer than that at x/D = 50 to the CT predictions, however, even at x/D = 100, the present contour values were higher than those from the CT simulations. This is an indication that the presently predicted flow in the gap region was not entirely fully-developed, even at the exit of the channel.

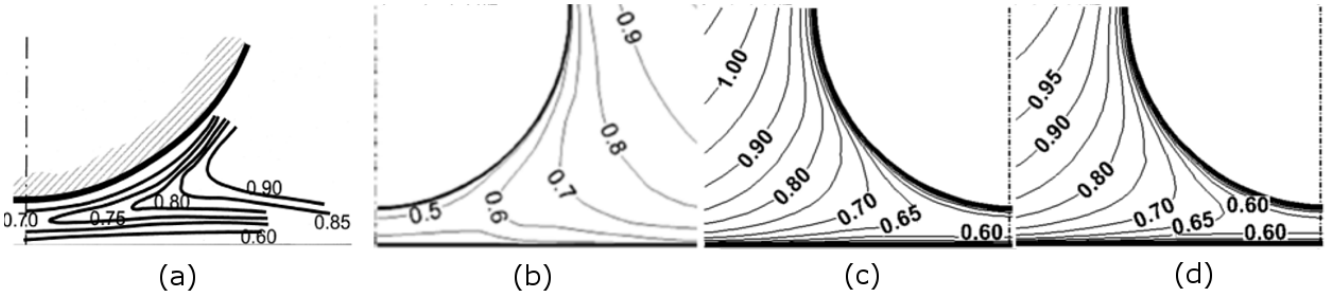

Figure 8. Isocontours of the time-averaged dimensionless axial velocity U/U_b in the gap region: (a) GT experiments; (b) CT simulations; present simulations at (c) $x/D = 50$ and (d) $x/D = 100$.

Figure 9 shows profiles of time-averaged dimensionless axial velocity in two planes: the symmetry plane below the rod and the equidistant plane. For each plane, this figure shows profiles at x/D = 30, 50, and 100, from which one may assess the degree of flow development in the gap between the rod and the bottom wall. In the symmetry plane below the rod (Fig. 9a) the maximum axial velocity at $x/D = 50$ increased by 88.7% compared to the value at x/D = 30, and then decreased by 2.6% at $x/D = 100$. This significant velocity change between x/D = 30 and x/D = 50 is largely attributed to the development of cross-flows in the gap (Fig. 5c). The small velocity difference between the two downstream profiles indicates proximity to flow development. On the equidistant plane (Fig. 9b), all velocity profiles had their maxima in the open sub-channel and their minima in the middle of the gap. However, it is evident that the axial velocity distribution at x/D = 30 was quite different from those at x/D = 50 and 100, consistently with the previous observations. In addition, the axial velocity for $0.4 \le |z/D| < 1.0$ was smaller at x/D = 50 than at x/D = 30, because the gap vortex street slowed down the local flows in the open sub-channel adjacent to the gap region. There is also a small but visible difference between the velocity profiles at x/D = 50 and x/D = 100, again indicating proximity to, but not attainment of, full development.

Figure 10 shows the present predictions of the time-averaged turbulent kinetic energy as well as corresponding results of the GT experiments and the CT simulations. CT predicted an increase in the turbulent kinetic energy in the gap region, comparable in level to the measurements, which they explained as the result of the gap vortex street. However, in the open channel, CT predicted that the turbulent kinetic energy was minimum on the symmetry plane above the rod (Fig. 10b), whereas GT found two minima, one in each open channel half way between the symmetry plane and the side wall (Fig. 10a). In the present simulations, the minimum of the turbulent kinetic energy at x/D = 50 (Fig. 10c) was in the open channel, in qualitative agreement with experiments (Fig. 10a), but its value was significantly lower than the experimental one. The low predicted turbulence level at x/D = 50 could be due to an insufficient level of the specified turbulence intensity at the inlet. To examine this, URANS simulations with higher inlet turbulence intensity were conducted. Details will be discussed in the later section. Furthermore, the predicted turbulent kinetic energy at x/D = 50 in the open channel toward the side walls differed from the experimental distribution. This difference is associated with the choice of the turbulence model, as will be discussed in a following section. Finally, the present simulations predicted a tendency of the turbulent kinetic energy minima in the open channels to shift toward the symmetry plane above the rod (Fig. 10d) as downstream distance increased, thus approaching the predictions of CT (Fig. 10b).

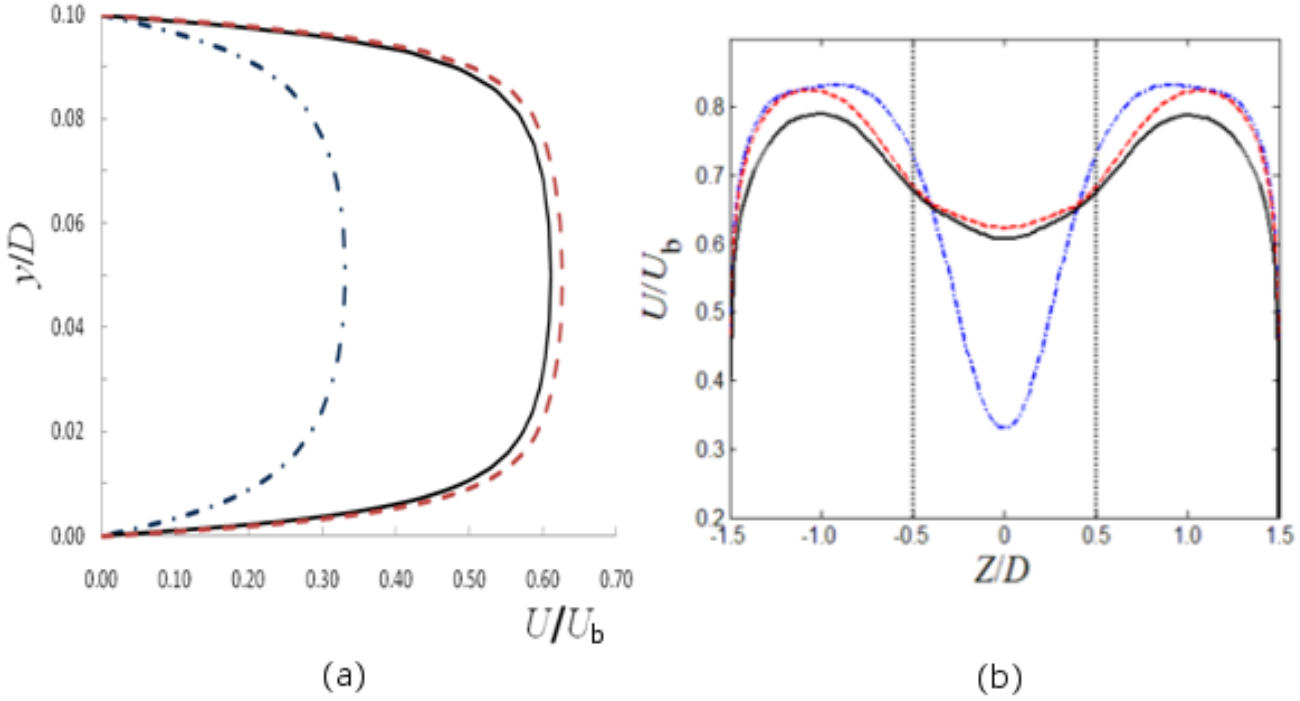

Figure 9. Time-averaged dimensionless axial velocity U/U_b at x/D = 30 (— · —), 50 (— —) and 100 (——) (a) on the symmetry plane in the gap; (b) in the equidistant plane located below the rod; dotted lines (·····) represent the projection of the rod on the equidistant plane.

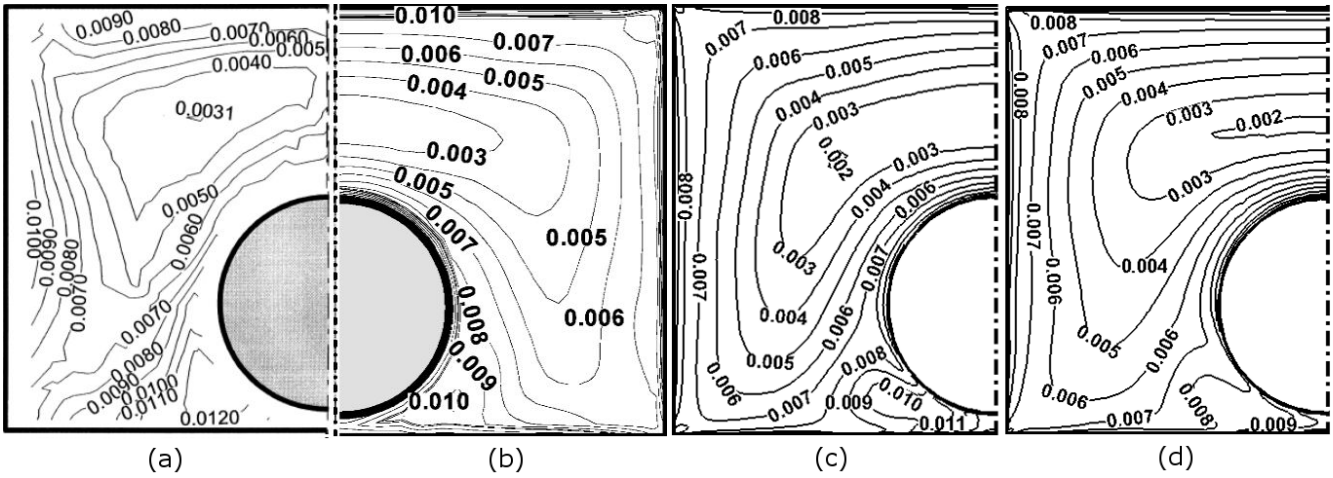

Figure 10. Isocontours of the time-averaged dimensionless turbulent kinetic energy k/U_b^2: (a) GT experiments; (b) CT simulations; present simulations at (c) x/D = 50 and (d) x/D = 100.

Figure 11 shows the turbulent kinetic energy distributions in the gap region for the present and the CT simulations. Both simulations show that the turbulent kinetic energy of 0.008 bulged away from the gap. The contour levels are comparable in magnitude, but somewhat different in shape, which may be due partially to plotting artefacts.

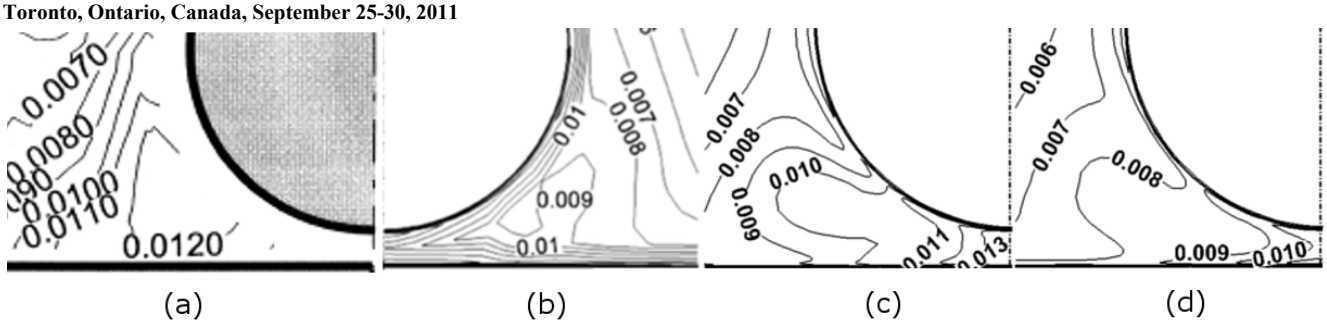

Figure 11. Isocontours of the time-averaged dimensionless turbulent kinetic energy k/U_b^2 in the gap region; (a) GT experiments; (b) CT simulations; present simulations at (c) x/D = 50 and (d) x/D = 100.

Figure 12 shows the variations of the time-averaged dimensionless turbulent kinetic energy on the equidistant plane and the time-averaged skin friction coefficient $C_f = \tau_w/(\rho U_b^2/2)$ (τ_w is the time-averaged local wall shear stress) around the rod. Figure 12a clearly documents the strong effect that the gap vortex street has on the turbulence level in the gap region: in the absence of a vortex street ($x/D = 30$), the turbulent kinetic energy has a very low minimum on the symmetry plane; in contrast, following development of the vortex street (x/D = 50 and 100), it has a pronounced maximum at the same location, due largely to the strong spanwise velocity fluctuations (Figs 3a and 5a). The weak local maxima on either side of the symmetry plane at x/D = 50 and 100 are due to locally higher levels of the axial velocity fluctuations. Curiously, the turbulent kinetic energy at x/D = 50 was higher than that at x/D = 100; this is probably the result of increasing spanwise separation of the vortices with increasing distance from their location of inception. The variation of the mean skin friction coefficient around the rod is presented in Fig. 12b. On the side of the rod facing the narrow gap, near $\phi = 0$ deg, the skin friction coefficient at $x/D = 30$ was very small, but it roughly tripled further downstream, as cross-flows became established; On the symmetry plane below the rod, C_f was 0.0033 at $x/D = 50$ and 0.0030 at $x/D = 100$, which are comparable to the CT value of 0.0033, but significantly lower than the measured value of 0.0050. On the side of the rod facing the wide gap, near $\phi = \pm 180$ deg, the trends of C_f in the domain of the gap vortex street were opposite to those in the narrow gap; this may be attributed to the shift of the maximum turbulent kinetic energy from the open channels (x/D = 50), towards the symmetry plane above the rod (x/D = 100).

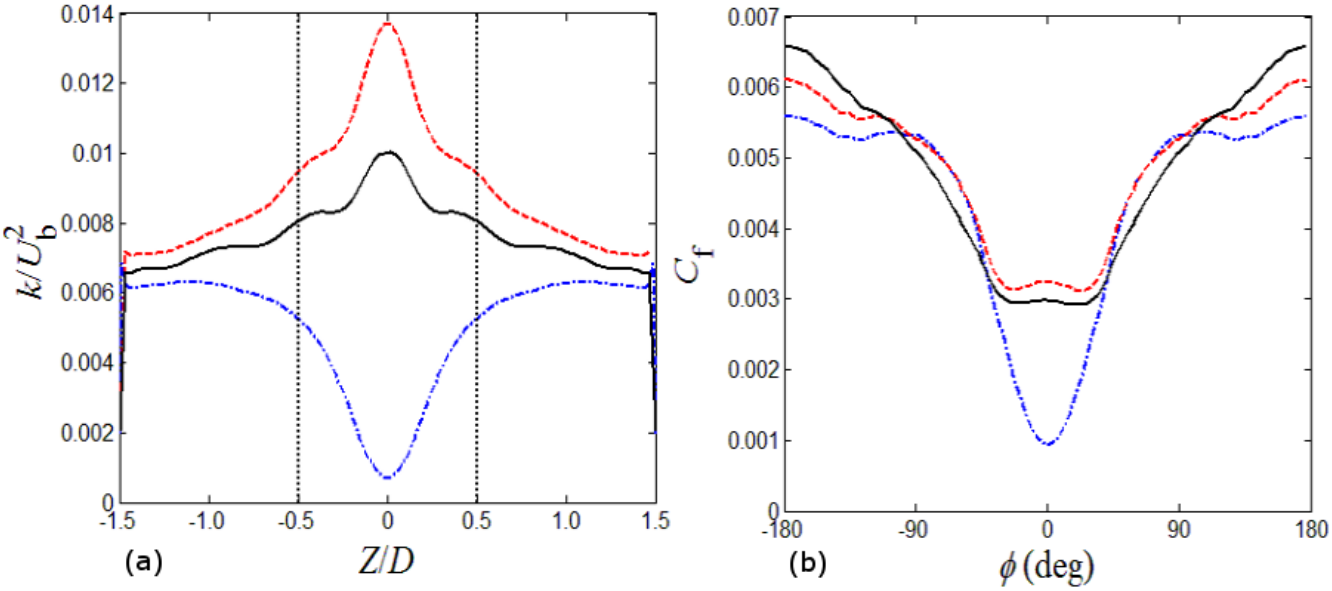

Figure 12. (a) Time-averaged dimensionless turbulent kinetic energy on the equidistant plane; dotted lines (·····) mark the projection of the rod; (b) Time-averaged skin friction coefficient around the rod; in both figures, x/D = 30 (— · —), 50 (— —) and 100 (——).

3.2 Comparison of unsteady developing flow simulations with two different inlet turbulence intensities

In the previous section, it was shown that URANS simulations with RSM-ε and a uniform inlet velocity underpredicted the turbulent kinetic energy in the open channel. We conjectured that this low turbulent kinetic energy might be associated with the specification of low turbulence intensity at the inlet. In order to test this possibility, we performed URANS simulations under the same conditions with the only difference that the specified inlet turbulence intensity was 10% rather the previous value of 3%.

Figure 13 shows predicted contours of the time-averaged axial velocity at x/D = 50 for both present simulations as well as measured velocity contours. In all present simulations, the predicted contours are very close to each other in shape and values. The percent difference of the maximum velocities in the open channel between the two simulations is about 0.8%. This closeness between the two predictions is evidence of the relative insensitivity of the mean velocity distributions at x/D = 50 to the inlet turbulence intensity. Figure 14 shows predicted and measured contours of the time-averaged axial velocity in the gap region. The predicted axial velocities in the gap region for the two cases are also close to each other. Although not shown here, the predicted axial velocity distributions at x/D = 100 for the two cases were found to be even closer to each other than the ones at x/D = 50. In conclusion, the effect of the inlet turbulence intensity specification on the mean flow in this duct is very weak and may be neglected in engineering analyses.

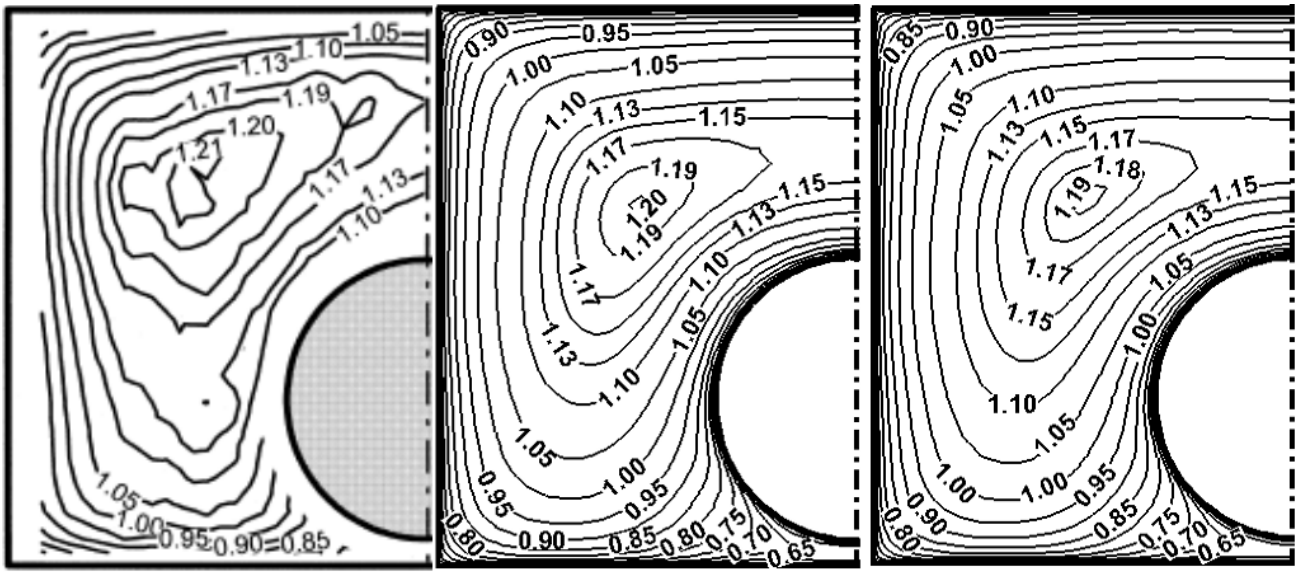

Figure 13. Isocontours of the time-averaged dimensionless axial velocity U/U_b at x/D = 50: (a) GT experiments; present simulations with inlet turbulent intensity of (b) 3% and (c) 10%.

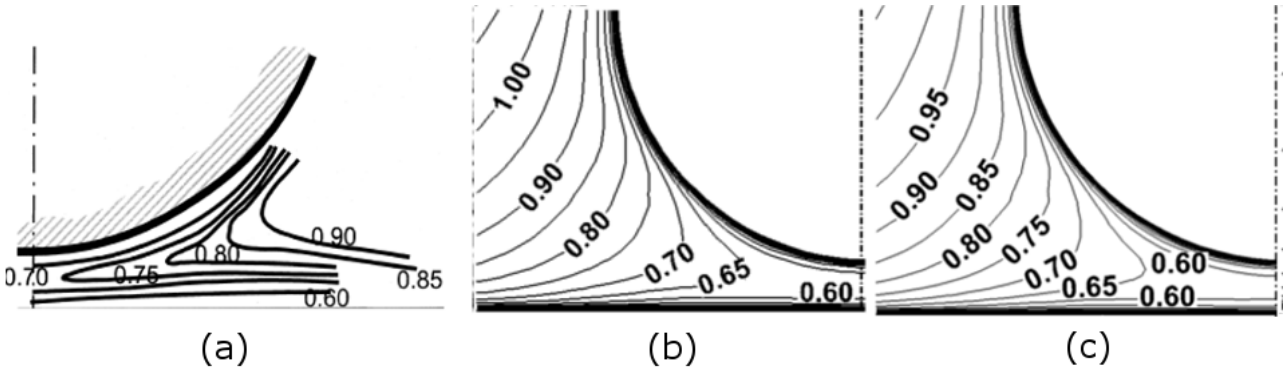

Figure 14. Isocontours of the time-averaged dimensionless axial velocity U/U_b in the gap region at x/D = 50: (a) GT experiments; present simulations with inlet turbulent intensity of (b) 3% and (c) 10%.

Figure 15 shows predicted contours of the time-averaged turbulent kinetic energy at x/D = 50 for two different inlet turbulence intensities. The measured contours for the GT experiments are also shown for comparison. The two sets of predicted contours have comparable levels, but slightly different shapes, especially in the open channels and in the large gap between the top wall and the rod. The low kinetic energy regions, as indicated by the areas enclosed by the contours marked by 0.002 and 0.003, are somewhat larger for the high inlet turbulence case than for the low inlet turbulence case, which is contrary to our expectation. Figure 16 shows time-averaged turbulent kinetic energy contours in the gap region. The differences between the two predictions are quite small and obscured by the contour generation process. In conclusion, the effect of inlet turbulence intensity on the turbulent kinetic energy distribution downstream of the inlet is also very weak. If at all, increasing the inlet turbulence level reduced slightly the downstream turbulent kinetic energy and so the underprediction of the turbulent kinetic energy by URANS analysis cannot be attributed to the specification of turbulence intensity at the inlet.

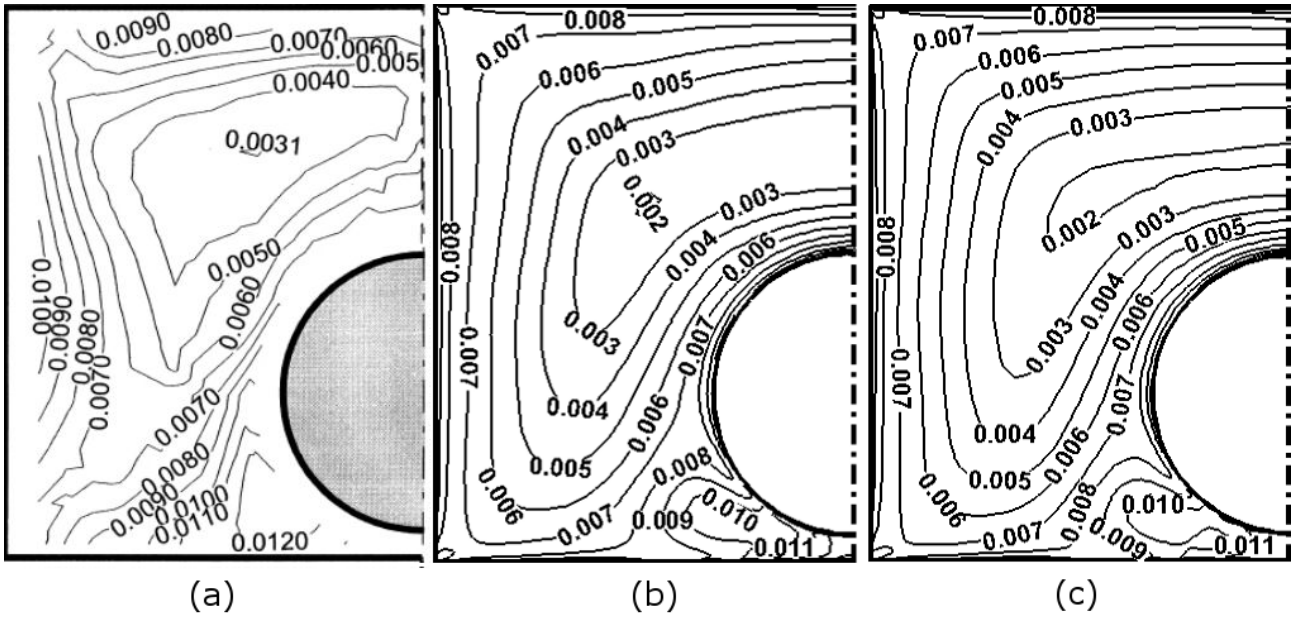

Figure 15. Isocontours of the time-averaged dimensionless turbulent kinetic energy k/U_b^2 at x/D = 50: (a) GT experiments; present simulations with inlet turbulent intensity of (b) 3% and (c) 10%.

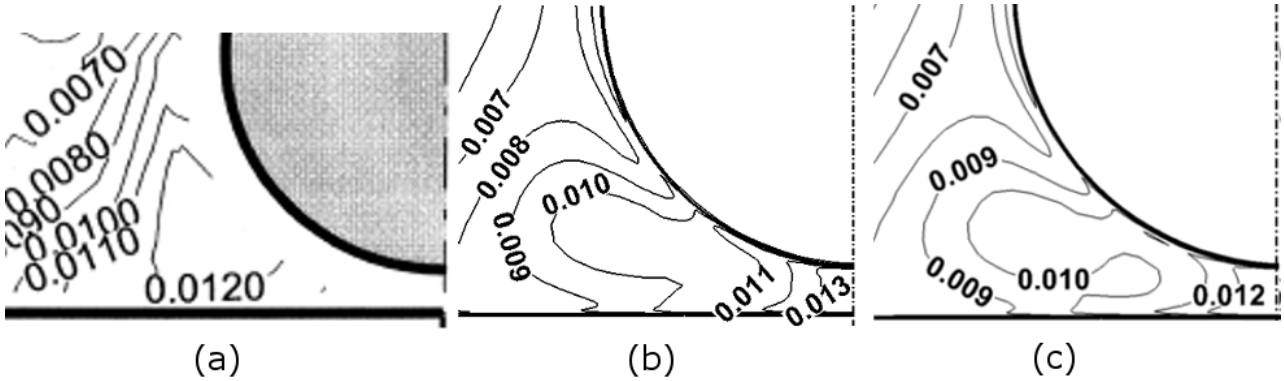

Figure 16. Isocontours of the time-averaged dimensionless turbulent kinetic energy k/U_b^2 in the gap region at x/D = 50: (a) GT experiments; present simulations with inlet turbulent intensity of (b) 3% and (c) 10%.

3.3 Comparison of URANS and RANS simulation results

Although there is plenty of evidence that RANS simulations have failed to predict accurately turbulent flows in tightly packed rod bundles, recent literature continues to include such studies. The main advantage of such simulations is their much shorter computing time by comparison to URANS and LES. In this section, we shall compare the results of RANS simulations with the RSM-ε model with corresponding predictions using URANS with the same turbulence model and same all other numerical settings. In our previous discussion about turbulence models, we explained that the RSM are preferable over two-equation models for rod bundle flows, because the latter cannot resolve the strong turbulence anisotropy in the gap region. Nevertheless, the k-ε model remains in use by some researchers of rod bundle flows, because of its relative stability and lower computational time compared to RSM. To

determine the effect of turbulence model in RANS of rod bundle flows, we have also conducted RANS simulations with the *k*-*ε* model.

Figure 17 shows isocontours of the dimensionless axial velocity at x/D = 50 for the URANS simulations with the RSM-*ε* model and RANS simulations with two different turbulence models. Measured contours for GT experiments are also shown in the figure. In the open channel, the corresponding contours for the RANS/RSM-*ε* (Fig. 17c) and URANS simulations (Fig. 17b) are very close to each other in shapes and positions. However, the contour shapes for the RANS/*k*-*ε* case are visibly different from those for the two RSM-*ε* cases, especially in the lower half of the open channel, where the contours are shifted towards the bottom wall and the gap, and in the large gap between the top wall and the rod, where the contours are shifted away from the top wall and the rod. The locations of the predicted velocity maximum were comparable for all three cases, approximately half way between the side wall and the symmetry plane; the maximum normalized velocity values were very close to each other (1.201 for the URANS, 1.200 for the RANS/RSM-*ε*, and 1.195 for the RANS/*k*-*ε* simulations). In summary, as far as the prediction of mean velocity distribution in the open channel is concerned, differences between URANS and RANS with the RSM-*ε* are within the experimental uncertainty, whereas the use of *k*-*ε* introduced some small but systematic differences from the two other cases.

Figure 18 shows axial velocity contours focused in the gap region for all present simulations and the GT measurements. The predicted axial velocity for the RANS/RSM-*ε* case is lower than that for the URANS case; for example, in the gap centre, the RANS prediction is nearly half that of the URANS prediction, which itself is about 15% lower than the experimental value. The RANS/*k*-*ε* simulations oddly underpredicted the centre-gap velocity by less than 20% compared to URANS. These results show that RANS simulations are inferior to URANS for calculating axial velocities in the gap region.

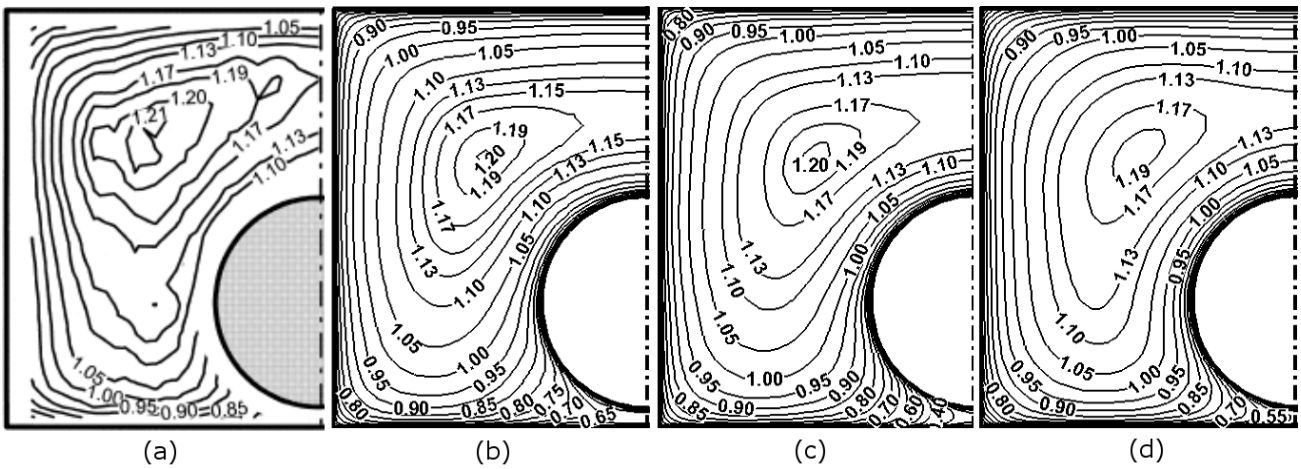

Figure 17. Isocontours of the dimensionless axial velocity U/U_b at x/D = 50: (a) GT experiments; (b) URANS simulations with RSM-*ε*; (c) RANS simulations with RSM-*ε*; (d) RANS simulations with *k*-*ε*.

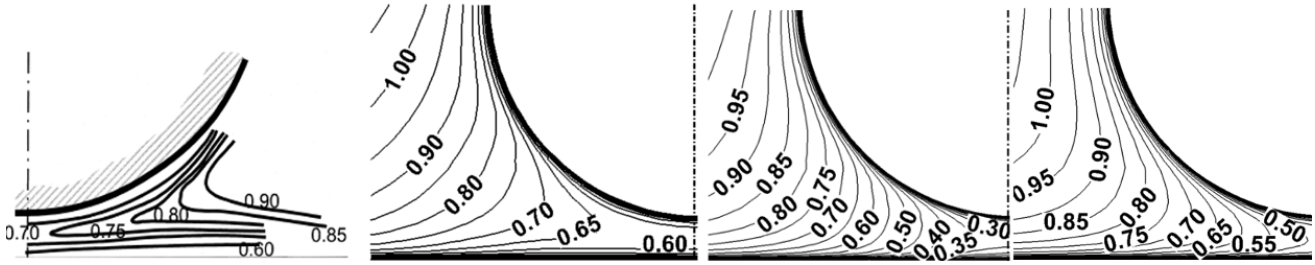

Figure 18. Isocontours of the time-averaged dimensionless axial velocity U/U_b in the gap region at x/D = 50: (a) GT experiments; (b) URANS simulations with RSM-ε; (c) RANS simulations with RSM-ε; (d) RANS simulations with k-ε.

Figure 19 shows the normalised turbulent kinetic energy at x/D = 50 for the GT experiments and the URANS and RANS simulations. In the open channel, the RANS/RSM-ε predictions are very close to the URANS predictions. Both simulations have their minima at about half way between the side wall and the symmetry plane. The minimum values were 0.00198 for the RANS and 0.00206 for the URANS, both being about 30% lower than the experimental value. Thus, as for the mean velocity, unsteady effects on the turbulent kinetic energy are negligible in the open channel away from the narrow gap. In contrast, the RANS/k-ε predictions, with a minimum value of 0.00154, are much lower than those for the other cases; the RANS/k-ε predictions also fail to predict the bulging of contours towards the upper left corner, as a result of their failure to account for secondary flows caused by turbulence anisotropy near the corner.

Figure 20 shows details of the normalised turbulent kinetic energy contours in the gap region. It is evident that the URANS/RSM-ε predicted to a large extent the measured increase in the turbulent kinetic energy in the gap region, but the two RANS simulations had notable differences from the GT measurement and the URANS simulations in terms of both levels and shapes of contours of turbulent kinetic energy. In the centre of the gap, the corresponding values were approximately 0.012 for the experiments, 0.0129 for the URANS (7% higher than the GT value), 0.00076 for the RANS/RSM-ε (94% lower than the GT value), and 0.00149 for the RANS/k-ε simulations (88% lower than the GT value). It is clear that, although URANS/RSM-ε predicted fairly well the experimental kinetic energy in the gap, both RANS completely failed in this respect.

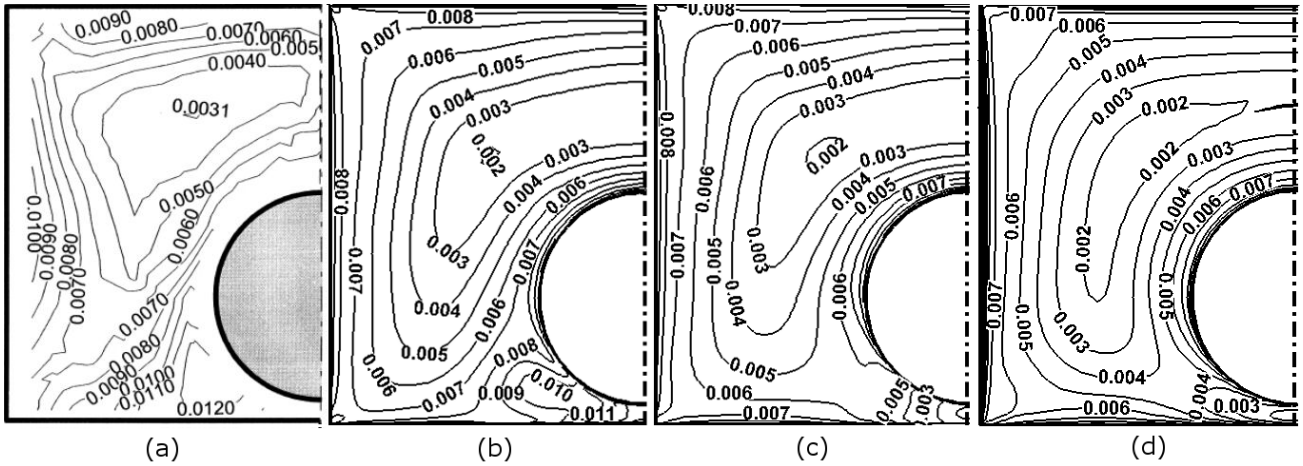

Figure 19. Isocontours of time-averaged dimensionless turbulent kinetic energy k/U_b^2 at $x/D = 50$: (a) GT experiments; (b) URANS simulations with RSM-ε; (c) RANS simulations with RSM-ε; (d) RANS simulations with k-ε.

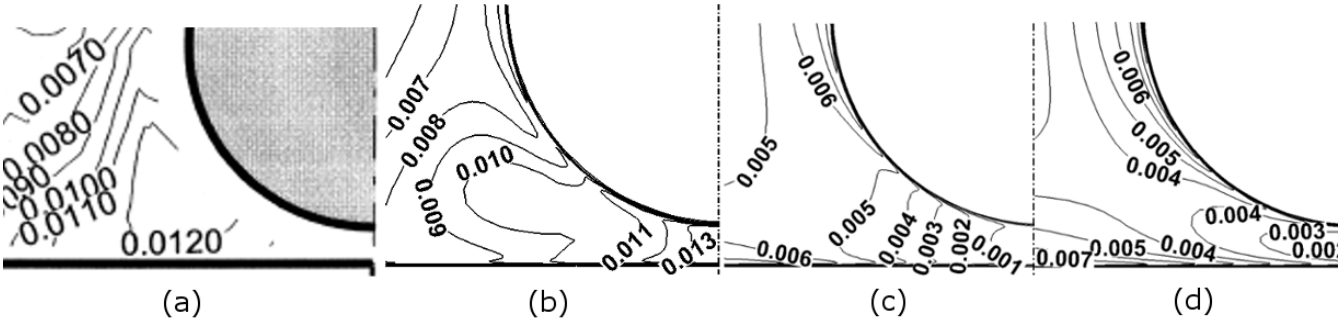

Figure 20. Isocontours of dimensionless turbulent kinetic energy k/U_b^2 in the gap region at $x/D = 50$: (a) GT experiments; (b) URANS simulations with RSM-ε; (c) RANS simulations with RSM-ε; (d) RANS simulations with k-ε.

3.4 Unsteady simulations of developing flow with a developed inlet velocity distribution

In this section, we report results of developing flow simulations with an inlet velocity distribution that matched the time-averaged velocity distribution at $x/D = 100$ in the simulations with the uniform inlet velocity that were reported in section 3.1. The same mesh and turbulence model were used in both cases. The objective of these simulations was to examine whether the characteristics of the gap vortex street and the downstream mean velocity and turbulence distributions were sensitive to the inlet velocity distribution.

Figure 21 shows a typical instantaneous streamwise profile of the cross-stream velocity along the centreline of the gap. In this instantaneous profile, no cross-flow oscillations are visible for $x/D < 15$, whereas, in the range $15 < x/D < 35$, strong oscillations built up, which persisted to the exit. This observation is consistent with the expectation that the use of a developed inlet velocity profile would shorten the downstream distance for the onset of gap instability, because in this case velocity distributions with azimuthal inflection are present right from the inlet onwards, as opposed to the case with uniform inlet velocity, in which inflection builds up gradually. The amplitude of these oscillations

reached a peak of $0.18U_b$ at $x/D = 36$, and for $53 < x/D$ it settled at a value of roughly $0.15U_b$. An average wavelength of $6.7D$ could be calculated from 7 peaks in the range $53 < x/D < 100$. This is much higher than both of the GT experimental value and the CT prediction, as well as the prediction with the uniform inlet velocity profile. The standard deviation of cross-flow velocity is also shown in Fig. 21. This parameter reached a mild peak of 0.13 at $x/D = 33$ and for $43 < x/D$ it settled at a value of roughly $0.11U_b$. These values are not very different from those in the simulations with the uniform inlet velocity. The Strouhal number was 0.11 at both $x/D = 50$ and 100, much lower than the values in all other simulations, as well as the experiments. These observations show that the use of a developed inlet velocity profile resulted in unrealistic predictions of the vortex street wavelength and frequency, although the reasons for this are not evident.

Figure 22 compares predicted contours of time-averaged axial velocity with those predicted by CT. The corresponding contours at $x/D = 50$ and $x/D = 100$ were quite close to each other as well as to the CT results, which demonstrates that flow development was faster in the case with the developed inlet velocity distribution than the case with the uniform inlet velocity. This is consistent with expectations, but one must also emphasize that the velocity distribution depends strongly on the gap vortex street effects and that the gap vortex street was not imposed on any of these cases but was generated spontaneously by the gap instability mechanism. An earlier inception of the gap vortex street is consistent with an earlier attainment of flow full development.

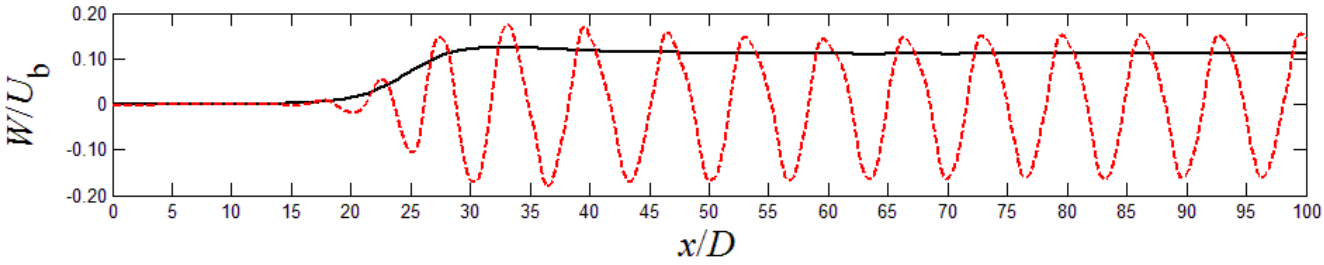

Figure 21. A typical instantaneous streamwise profile of the cross-flow velocity along the gap centreline (– –) and the standard deviation of local cross-flow fluctuations (——).

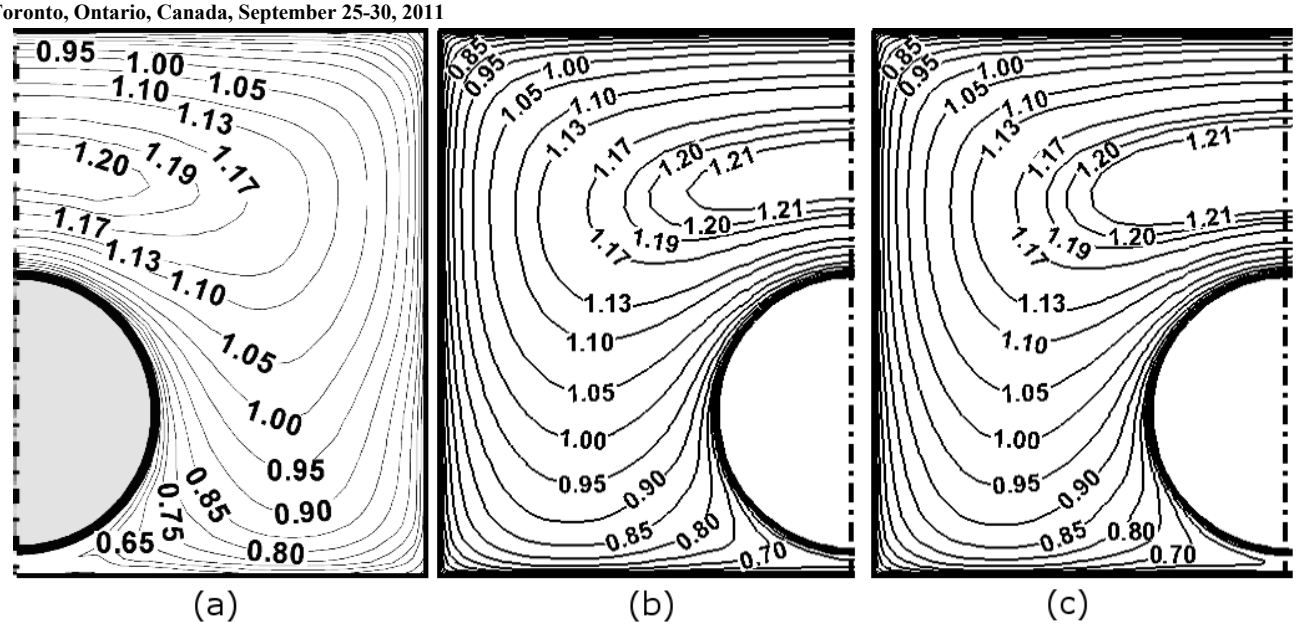

Figure 22. Isocontours of the time-averaged dimensionless axial velocity U/U_b: (a) CT simulations; present simulations with developed inlet velocity at (b) x/D = 50 and (c) x/D = 100.

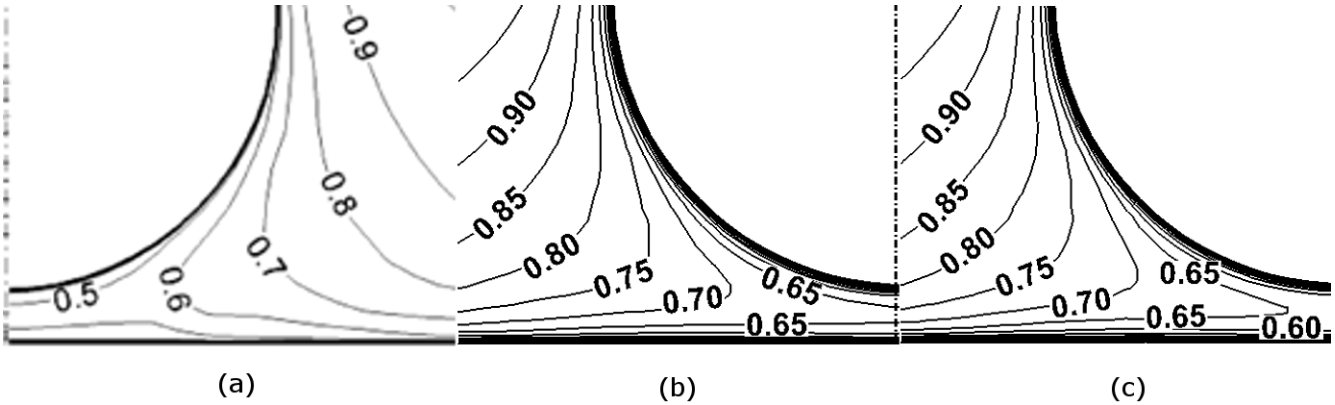

Figure 23. Isocontours of the time-averaged dimensionless axial velocity U/U_b in the gap region: (a) CT simulations; present simulations with developed inlet velocity at (b) x/D = 50 and (c) x/D = 100.

Figure 23 shows detailed views of the predicted axial velocity contours in the gap region below the rod, which were compared with contours of the CT simulations. It is seen in Figs. 23b and 23c that the axial velocity between two cross-sections at x/D = 50 and x/D = 100 were different in the gap region. It demonstrates that flow development was in process in the gap region. Both contour values were higher values than those from the CT simulations.

Figure 24 shows turbulent kinetic energy contours for the present simulations at x/D = 50 and 100, as well as the ones by CT. In general, in all three cases the contours were very close to each other in shape and values and they all had a single minimum on the symmetry plane above the rod and a single maximum in the middle of the gap.

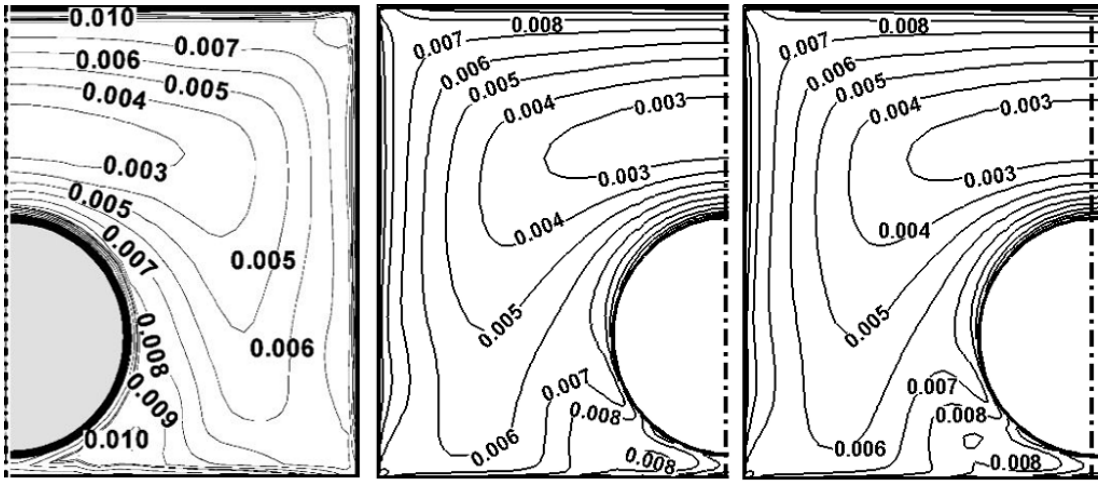

Figure 24. Isocontours of the time-averaged dimensionless turbulent kinetic energy k/U_b^2: (a) CT simulations; present simulations with developed inlet velocity at (b) x/D = 50 and (c) x/D = 100.

Two important conclusions can be based on the previous comparisons: first that the predictions of the gap vortex street spacing and frequency are quite sensitive to the inlet boundary condition; and second that the time-averaged mean velocity and turbulence distributions in two types of simulations can be close to each other, even if the vortex street spacings are different, as long as the strengths of the vortices are comparable.

3.5 Comparison of unsteady developing flow simulations with different turbulence models

In this section, we report the results of systematic investigations of the performance of different turbulence models in rod bundle flows, as evidenced by their predictions of the gap vortex street and the distributions of the mean axial velocity and turbulent fields in the present channel. In all cases, unsteady simulations of a developing flow with a uniform inlet velocity were performed; the computational mesh was kept the same for all cases, except when a refinement was dictated by the resolution requirements of a particular model. Five turbulence models have been considered: URANS with RSM-ε, URANS with RSM-ω, SAS, IDDES and the segregated hybrid model. Whenever we present results from the LES sub-domain of the segregated hybrid model simulations, we shall refer to them as LES results.

Figure 25 shows typical instantaneous streamwise profiles of the cross-flow velocity along the gap centreline, as well as the corresponding local standard deviations, for the five different simulations. Flow oscillations across the gap for the URANS simulations first appeared at x/D = 37 for the RSM-ε and x/D = 35 for the RSM-ω. In contrast, such oscillations started significantly upstream, at about x/D = 13 for the SAS, IDDES, and LES. This difference between the two groups could be related to the method of turbulence specification at the inlet. For the URANS simulations, we specified a constant turbulence value, whereas the SAS, IDDES and LES employed modelling of the velocity fluctuations at the inlet. For the URANS group cross-flow oscillations were fairly regular, whereas for the second group the variations of amplitudes and wavelengths along the channel were relatively strong, and the latter profiles also had phase jumps and missing cycles.

Figure 26 shows both the computed curves, as well smoothened curves, of the power spectra of the cross-flow velocity fluctuations in the centre of the narrow gap. Because of the relatively short time available for spectral calculations, all spectra have a large scatter. As ensemble averaging was not possible for the same reason, we could only resort to frequency domain smoothing, which introduced considerable uncertainty of the spectral values as well as of the location and amplitude of the peak. The Burg algorithm, implemented in Matlab, was used to smoothen the power spectra. Two URANS smoothened spectra had relatively sharp peaks, where most of the spectral power was concentrated, whereas the other smoothened spectra, especially the one from the LES, had relatively wide peaks. Except for the LES spectrum, the other spectra had very high drop-off rates following the peak, which indicates that they contained negligible energy in the universal equilibrium range, namely in the inertial and viscous subranges. The LES spectrum was the only one that had appreciable energy in the high frequency range; in fact, the smoothened spectrum in the range $0.3 < fD/U_b < 0.9$ seemed to be compatible with the Kolmogorov -5/3 spectral law in the inertial subrange. Because of the large uncertainty in the spectral estimates, and in view of the high CFL number (12.54) and the large stretching ratio (1.2) in the LES zone, confidence in the high frequency spectral predictions of the LES remains limited, although such predictions are definitely superior to those obtained by any other model. In general, all observations concerning spectra are consistent with expectations based on well known capabilities and limitations of the corresponding turbulence models.

The average convection speed and wavelength of the gap vortex street predicted by the different turbulence models were estimated following the procedure used by GT. First, the streamwise space-time correlation coefficient of the spanwise velocity fluctuations W was calculated as

$$R_{ww}(\Delta x, \Delta t) = \frac{\sum_{i=1}^{N}\left[(W_i(x,t) - \overline{W}(x))(W_i(x+\Delta x, t+\Delta t) - \overline{W}(x+\Delta x))\right]}{\sqrt{\sum_{i=1}^{N}(W_i(x,t) - \overline{W}(x))^2}\sqrt{\sum_{i=1}^{N}(W_i(x+\Delta x, t+\Delta t) - \overline{W}(x+\Delta x))^2}} \quad (3)$$

Figure 27a is a representative plot of the space-time correlation coefficient vs. normalized time, whereas Fig. 27b shows the dependence of the time delay for maximum correlation upon streamwise separation. The normalized convection speed of the gap vortices was taken to be equal to the slope of a line fitted to the data in Fig. 19b and the normalized wavelength was taken to be the ratio of the normalized convection speed and the Strouhal number corresponding to the spectral peaks.

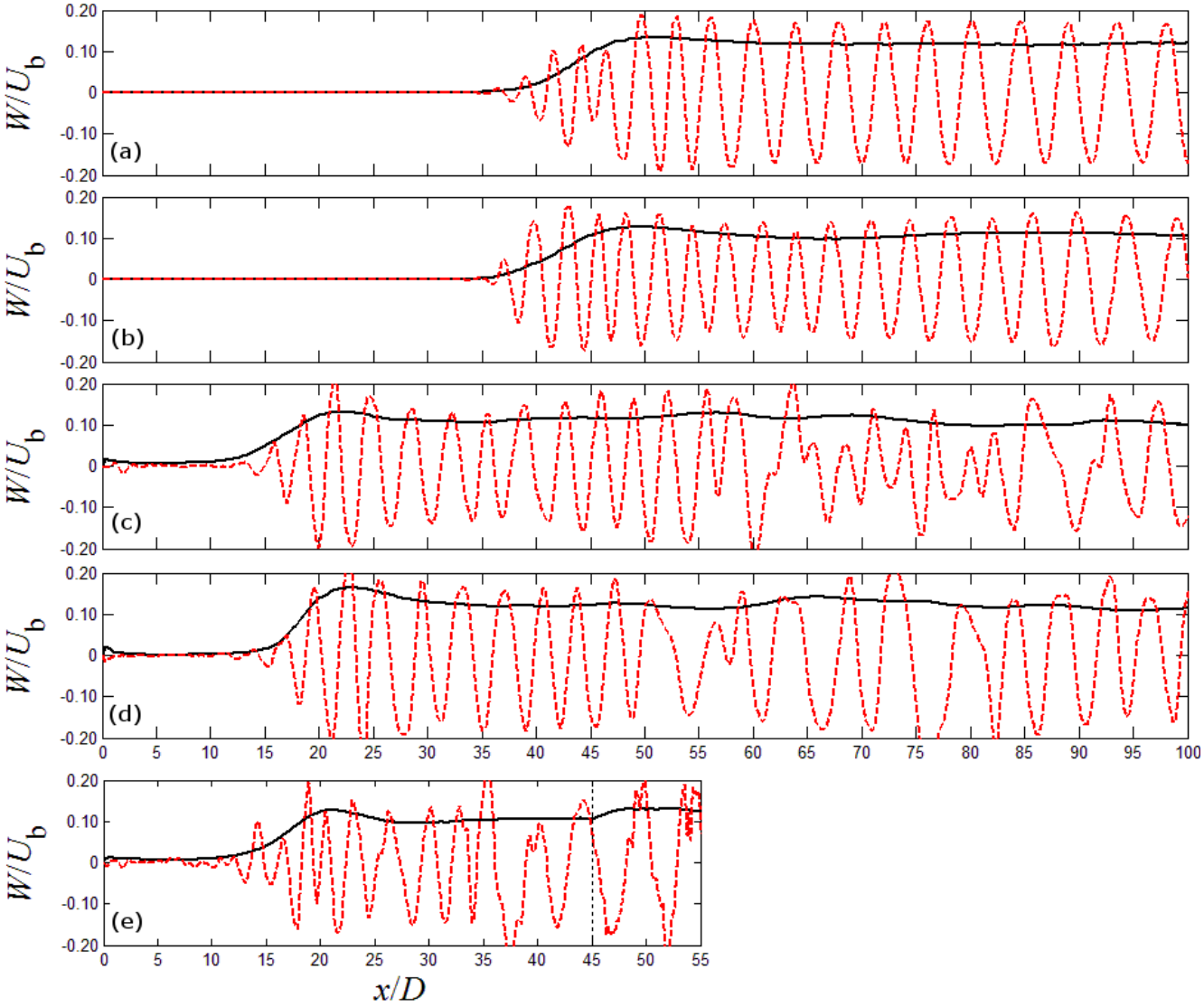

Figure 25. Typical instantaneous streamwise profiles of the cross-flow velocity along the gap centreline (– –) and standard deviations of local cross-flow fluctuations (——); (a) RSM-ε; (b) RSM-ω; (c) SAS; (d) DES; (e) segregated hybrid model (dashed line indicates the interface between the SAS and the LES sub-domains).

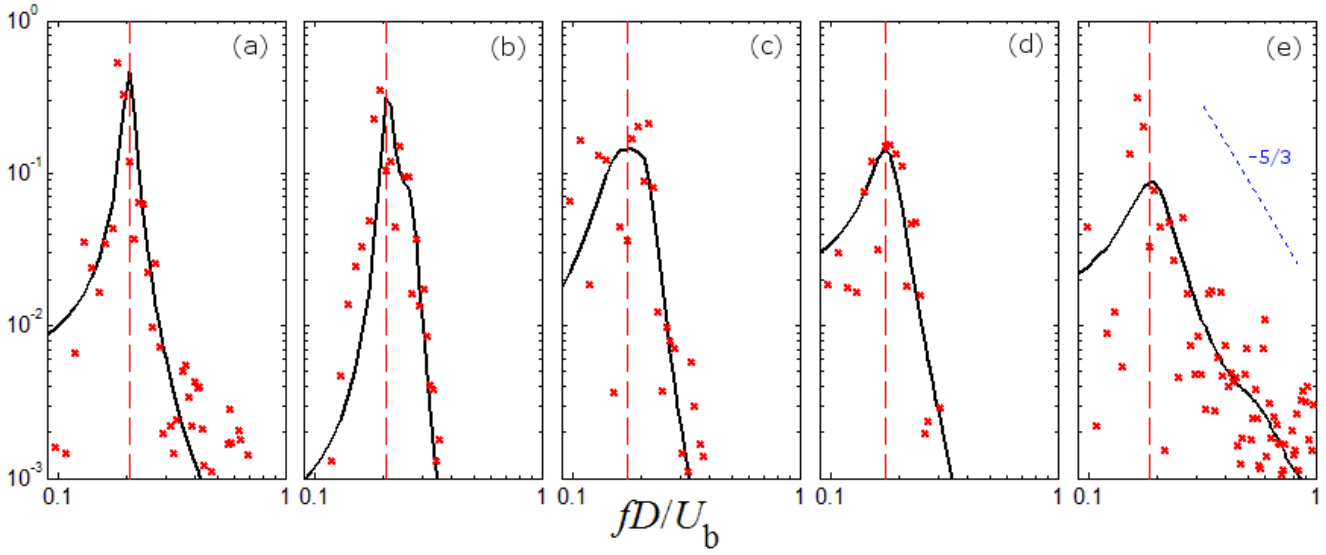

Figure 26. Predicted (×) and smoothened power spectral densities (——) of the spanwise velocity fluctuation in the centre of the gap at $x/D = 50$; (a) URANS with RSM-ε, (b) URANS with RSM-ω, (c) SAS, (d) IDDES, (e) LES; dashed lines (— —) indicate peak locations; the -5/3 line (·····) indicates the Kolmogorov spectral law in the inertial subrange.

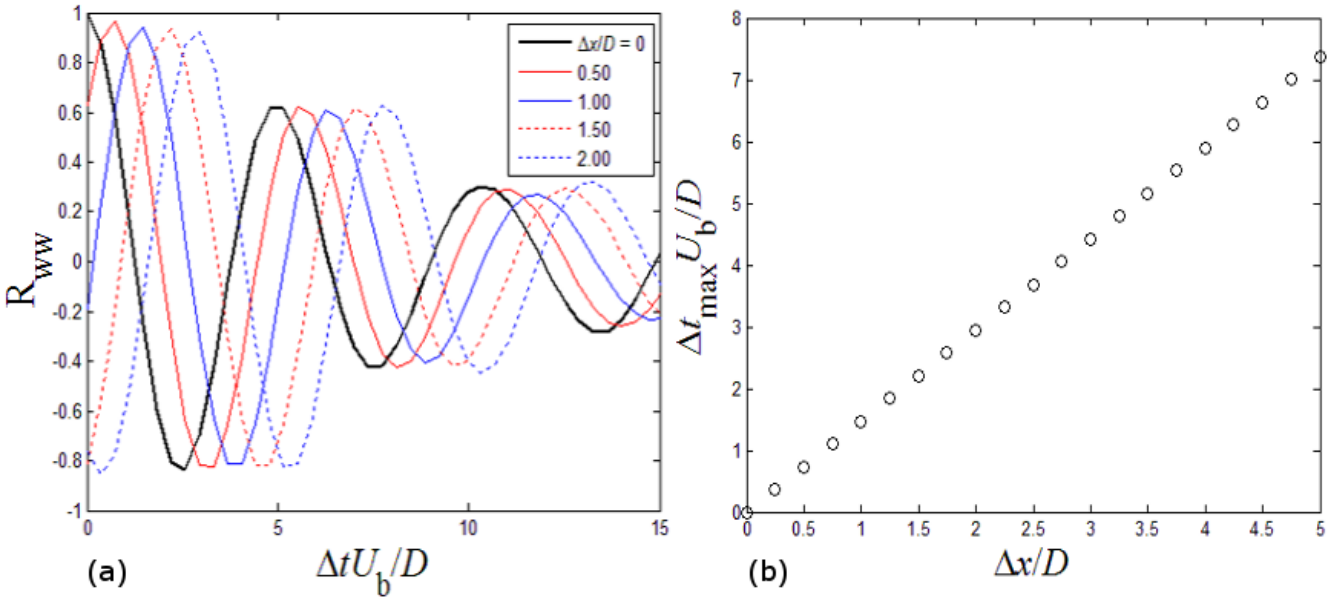

Figure 27. (a) Representative space-time correlation coefficient of cross-flow velocity along the gap centreline (URANS simulations with RSM-ε); (b) normalized time delay for maximum correlation vs. streamwise separation.

Table 2 summarizes the predictions of the gap vortex street characteristics at $x/D = 50$, as well as the corresponding GT and CT values. None of the present Strouhal number predictions was far from the experimental value; the two URANS predictions were about 17% higher, whereas the differences between the other three predictions and the GT value were within the estimated uncertainty limits. The CT estimate of Strouhal number, corresponding to an infinitely long channel, is distinctly higher than all other values and roughly 60% higher than the measurement. These observations clearly indicate that the CT overestimation of Strouhal number is not caused by an inherent inaccuracy of the

URANS method, but it is attributable to the use of the streamwise-periodic boundary condition, which is not very suitable for simulating the GT experiments. The convection speeds of the gap vortex street predicted by different models are also not too far from each other, although the LES prediction is the closest to the GT value and the RSM-ω prediction is also very close. All other predictions, including the one by CT, are underestimated, perhaps indicating weaker than measured gap vortex street effects in the gap region. The spacing between vortex pairs (vortex street wavelength) is predicted quite accurately by the LES, whereas it is underestimated by the other models and overestimated by CT.

Table 2 Characteristics of the gap vortex street at $x/D = 50$

	Strouhal number St	Convection speed of vortices U_c/U_b	Spacing between pairs of vortices λ/D
GT experiments	0.17	0.78	4.2
CT simulations	0.27	0.62	4.9
RSM-ε	0.20±0.02	0.68±0.05	3.4
RSM-ω	0.20±0.02	0.76±0.05	3.8
SAS	0.18±0.04	0.63±0.03	3.5
DES	0.17±0.02	0.63±0.03	3.7
LES	0.18±0.03	0.77±0.08	4.3

Figure 28 shows isocontours of the axial velocity in the channel cross-section at $x/D = 50$ for the GT experiments and the present simulations with five different turbulence models. All simulations reproduced the experimental bulge of velocity toward the gap region as well as the presence of a maximum velocity in the open channel. Among the simulations, those with the LES were the closest to the experiments, especially in the gap region. This is shown more clearly in Fig. 29, which presents details of the same contours in the gap region. The LES predicted a minimum velocity in the gap centre that was close to the experimental value of about 0.7, whereas all other models underpredicted this value.

Figure 30 shows isocontours of the predicted turbulent kinetic energy at $x/D = 50$ for the developing flow simulations using different turbulence models, together with GT measurements. In the open channel, the predictions of all models were lower than the experimental values. The shapes of the turbulent kinetic energy contours predicted by the LES were closest to the measured ones. Figure 31 shows details of the predicted turbulent kinetic energy in the gap region from all the simulations. Measurements are unavailable for this case. The highest turbulent kinetic energy was obtained from the LES.

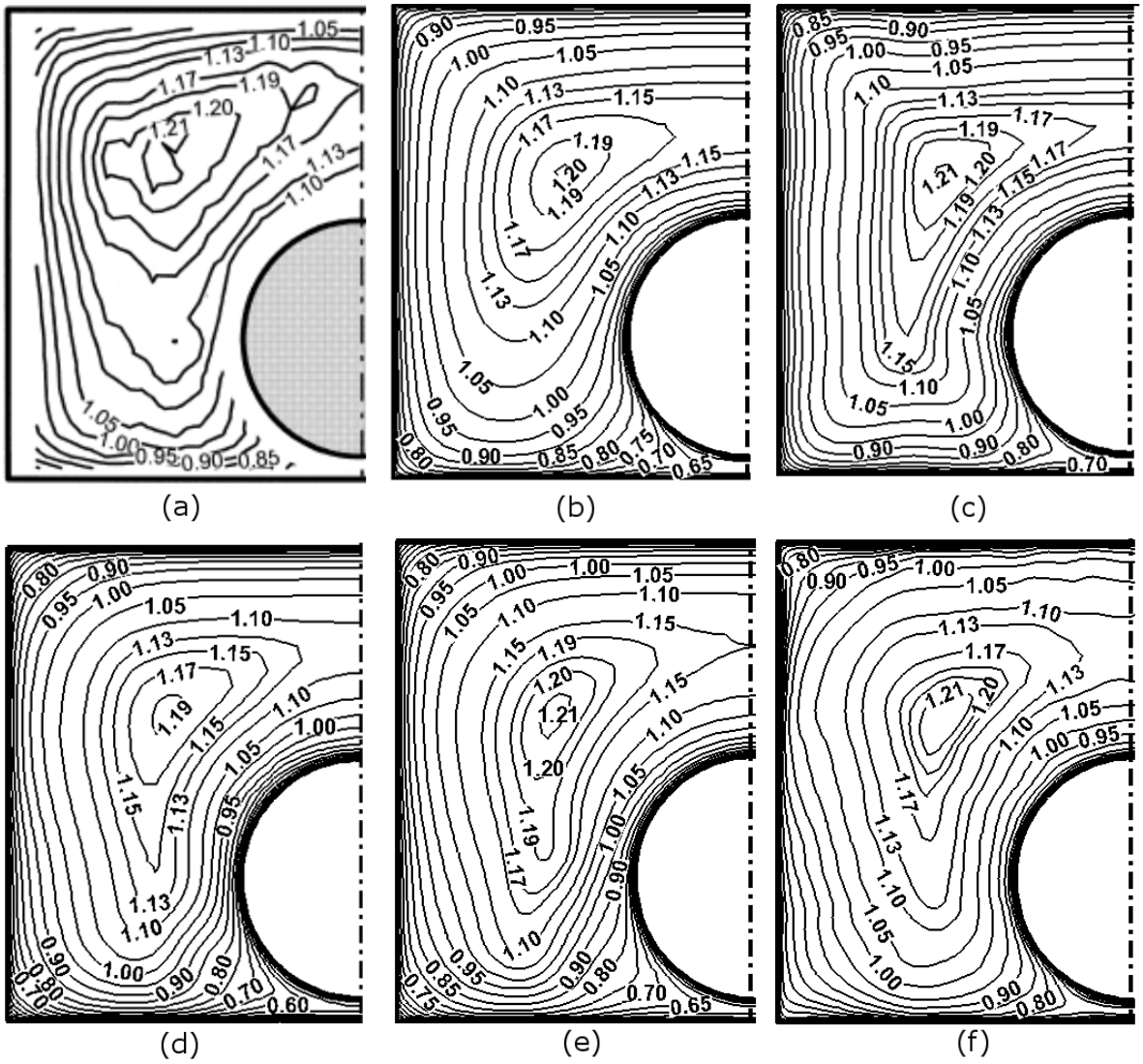

Figure 28. Isocontours of the time-averaged dimensionless axial velocity U/U_b at $x/D = 50$: (a) GT experiment; present simulations with (b) RSM-ε, (c) RSM-ω, (d) SAS, (e) IDDES, and (f) LES.

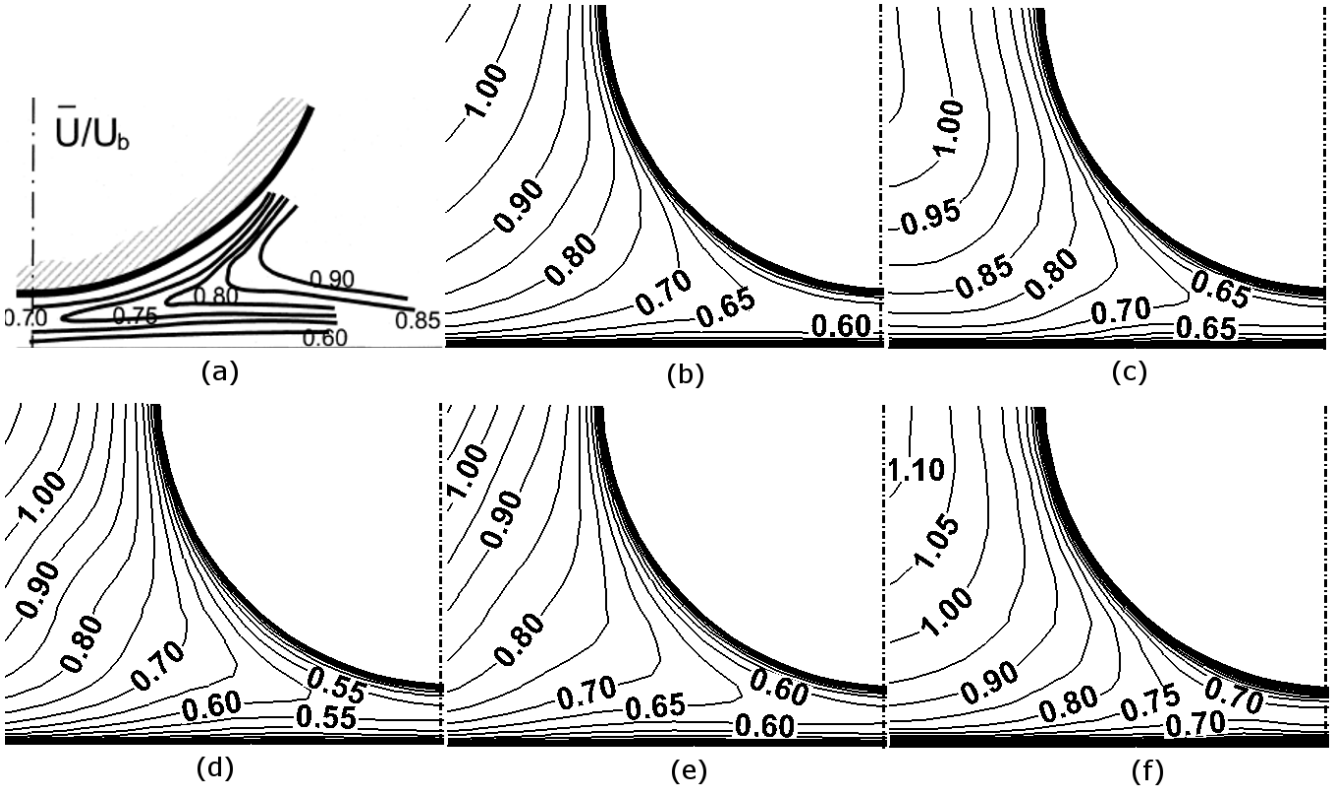

Figure 29. Isocontours of the time-averaged dimensionless axial velocity U/U_b in the gap region at x/D = 50: (a) GT experiment; present simulations with (b) RSM-ε, (c) RSM-ω, (d) SAS, (e) IDDES, and (f) LES.

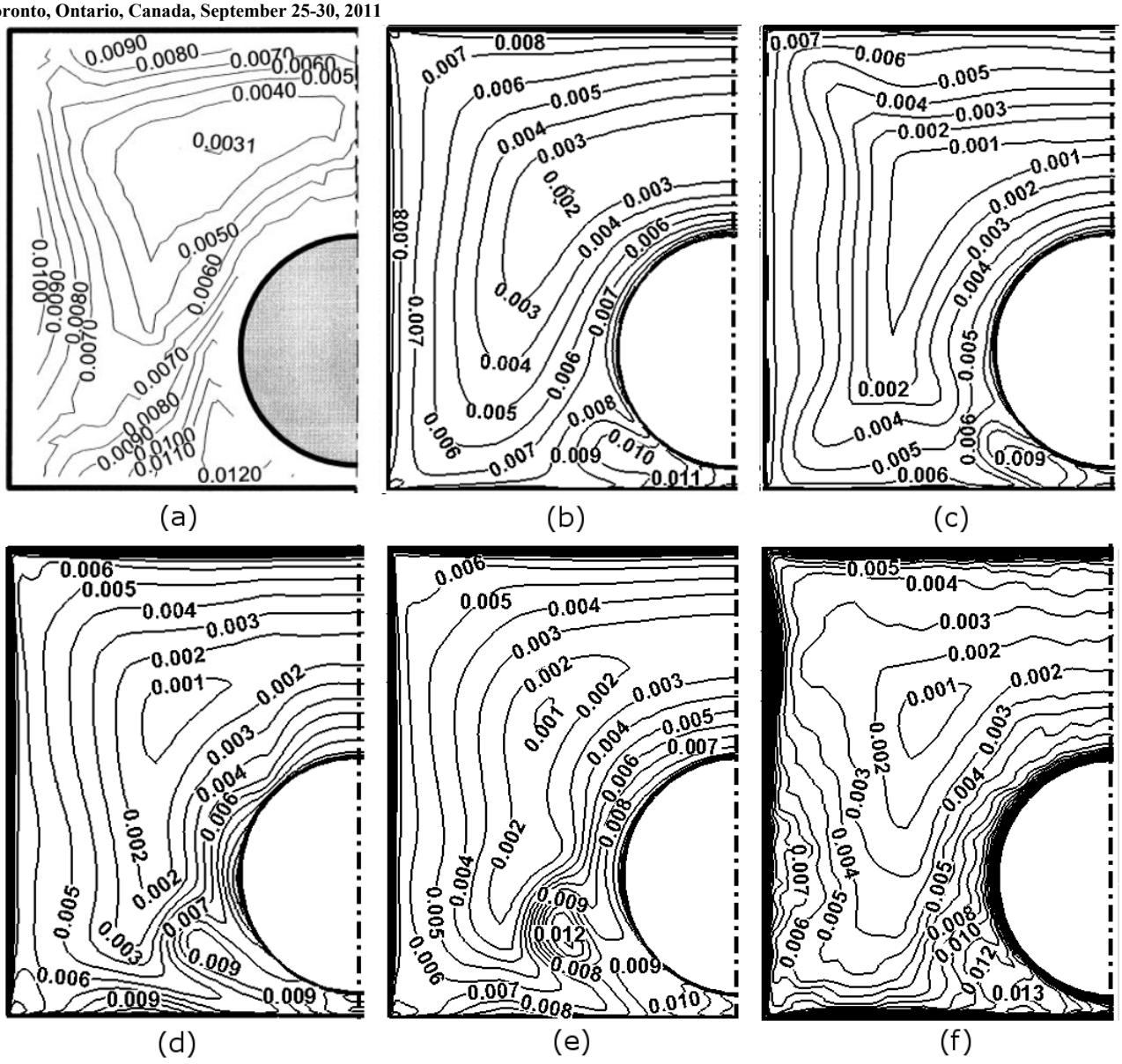

Figure 30. Isocontours of the time-averaged dimensionless turbulent kinetic energy k/U_b^2 at x/D = 50: (a) GT experiment; present simulations with (b) RSM-ε, (c) RSM-ω, (d) SAS, (e) IDDES, and (f) LES.

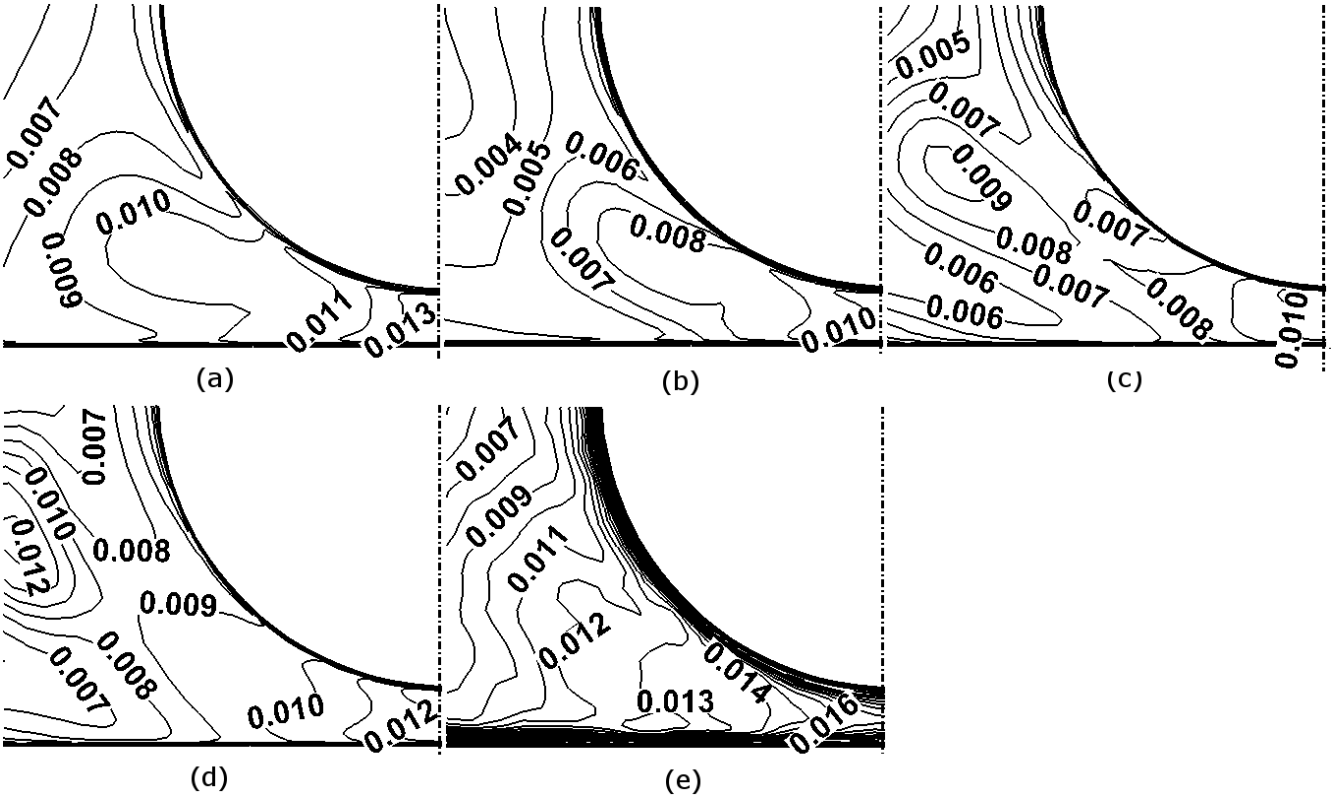

Figure 31. Isocontours of the time-averaged dimensionless turbulent kinetic energy k/U_b^2 in the gap region at $x/D = 50$: present simulations with (a) RSM-ε, (b) RSM-ω, (c) SAS, (d) IDDES, and (e) LES.

3.6 Unsteady Euler simulations

Unsteady Euler simulations with the developed inlet velocity distribution have been conducted for a developing flow in the present channel. The objective of this analysis was to investigate whether gap instability and a gap vortex street could occur even in the absence of viscosity.

Figure 32 shows an instantaneous streamwise profile and the local standard deviation of the cross-stream velocity along the centreline of the gap. It presents evidence of cross-flow oscillations in the gap region, even though their amplitudes and wavelengths differed widely from those of the URANS simulations. The standard deviation of the oscillations was growing in the range $17 < x/D < 50$, it reached a peak of $0.09U_b$ at $x/D = 51$, and for $76 < x/D$ it settled at a value of roughly $0.06U_b$, which is less than half the value of $0.13U_b$ in the URANS with the RSM-ε. Unlike all other developing-flow simulations, the amplitudes and wavelengths of the Euler simulations varied significantly along the channel.

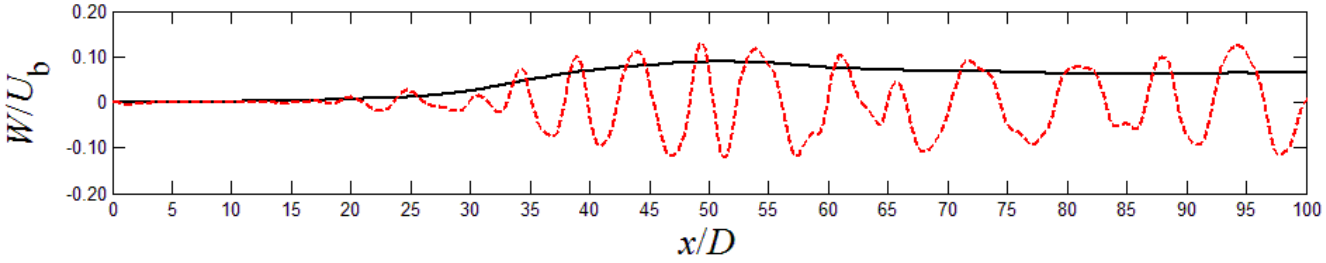

Figure 32. A typical instantaneous streamwise profile of the cross-flow velocity along the gap centreline (– –) and the standard deviation of local cross-flow fluctuations (——).

Figure 33 shows plots of the smoothened power spectral density against the dimensionless frequency at x/D = 50 and 100. Both curves had distinct peaks. As for the URANS simulations, the average Strouhal number was reduced downstream. At x/D = 50 and 100 it was, respectively, 0.13 and 0.11, with both values being significantly lower than the GT experimental value and the CT prediction, as well as values from the URANS with RSM.

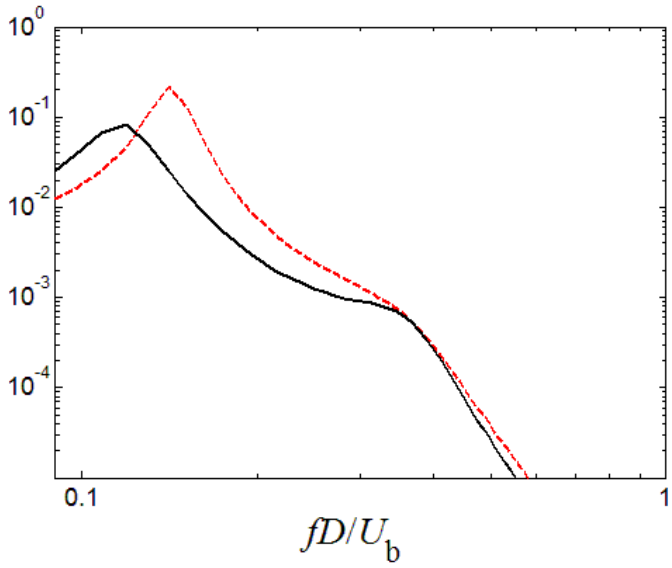

Figure 33. Power spectral density of the spanwise velocity fluctuation in the centre of the gap at x/D = 50 (– –) and 100 (——).

In summary, this study shows that gap instability and a gap vortex street can occur spontaneously (i.e., without forcing) and be maintained in an inviscid flow with an azimuthally inflected velocity distribution. The predictions of flow patterns from the inviscid analysis are inferior to those obtained by viscous analysis, not to mention that the inlet velocity distribution for a given channel cannot be obtained by inviscid analysis. Although this work contributes to our understanding of these important mechanisms in rod-bundle flows, it also demonstrates that inviscid flow analysis is not suitable for quantitative predictions of such flows.

4. Conclusions and closing remarks

Three-dimensional, unsteady simulations for developing turbulent flows in a rectangular channel containing a cylindrical rod have been performed to investigate their sensitivity to the choices of inlet boundary conditions and turbulence models. These effects have been examined by comparing the predicted distributions of the time-averaged velocity and turbulent kinetic energy in the entire channel and, particularly, in the gap region, as well as the characteristics of the predicted gap vortex streets with measurements by GT [5] and predictions by CT [21] which used the streamwise-periodic boundary condition.

The URANS simulations with RSM-ε and a uniform inlet velocity clearly demonstrated the onset of gap instability at some downstream location in the channel, following which strong cross-flow oscillations built up rapidly across the gap and then were maintained downstream in the form of a vortex street with nearly constant amplitude and wavelength. The Strouhal number of these oscillations was somewhat higher than the GT experimental value but significantly lower than the CT prediction. Downstream of the gap instability location, the time-averaged axial velocity in the middle of the gap nearly doubled and the turbulent kinetic energy had a maximum at that location, as opposed to a very low minimum that it had upstream of the instability location; moreover, the skin friction coefficient on the rod surface facing the narrow gap roughly tripled following the gap instability.

The URANS simulations with a 3% inlet turbulent intensity underpredicted the turbulent kinetic energy in the open channel. To test the possibility that this might be due to the low turbulence specification at the inlet, URANS simulations with a 10% inlet turbulent intensity were also performed. It was found that the effects of the inlet turbulence intensity specification on the mean flow and the turbulent kinetic energy far downstream of the inlet were very weak and so the underprediction of the turbulent kinetic energy by URANS simulations cannot be attributed to inlet specifications.

Results from RANS simulations were compared with those from URANS simulations under the same conditions. It is clear that the RANS simulations predict poorly the flow and turbulence distributions in the narrow gap region. Therefore, they are not recommended as a lower-cost substitute of URANS for flows in tightly packed rod bundles.

The effect of inlet velocity distribution was investigated by comparing results with a uniform inlet velocity and with a fully-developed inlet velocity distribution. The use of a developed inlet velocity shortened significantly the downstream distance for the onset of the gap instability, but the Strouhal number was much lower than the values from all other simulations and the GT experiment. These observations indicate that a uniform inlet velocity specification would be preferable.

A comparative analysis was made for the results of simulations using five turbulence models, namely URANS with two kinds of Reynolds stress models (RSM), one suggested by Launder and Shima (RSM-ε) and another suggested by Wilcox (RSM-ω), Scale Adapted Simulations (SAS), which are second generation URANS, as well as hybrid simulations of two kinds, namely Improved Delayed Detached Eddy Simulations (IDDES) and segregated hybrid model simulations. Despite their higher computational requirements, the RSM were chosen over two-equation or one-equation turbulence models, because the former are the only ones that can resolve the turbulence anisotropy in the gap region and the secondary flows in the corners of the channel. Both types of the URANS predicted fairly accurately the flow distributions and the characteristics of the gap vortex street; however, the SAS, IDDES and the segregated hybrid model predicted a shorter distance from the inlet for the onset of the

gap instability. Among all methods, the LES, employed in a downstream sub-domain of the channel as part of the segregated hybrid model simulations, reproduced most accurately the experimental results, particularly the characteristics of the gap vortex street as well as the time-averaged axial velocity and turbulent kinetic energy in the gap region. The LES analysis was the only one that predicted some fine turbulence structure embedded in the large-scale oscillations.

Unsteady inviscid (Euler) simulations with a developed inlet velocity distribution were also conducted in the present channel. These also predicted the onset of gap instability, which proves that this is an inviscid flow mechanism, associated with the azimuthally inflected velocity distribution. The predictions of this method differed very significantly from the measurements, and so unsteady Euler flow analysis is not recommended for rod-bundle-like flows.

In summary, although the LES method showed a superior accuracy in predicting the characteristics of the gap vortex street and the time-averaged flow field in the present simplified rod-bundle flow, URANS with RSM, when properly applied, also had a fair accuracy. Even when using a fairly powerful computer cluster with 48 threads over several months for a single simulation, we could only run a wall-layer resolving LES over a streamwise length of 10D for the simplest kind of a rod bundle at a Reynolds number that is markedly lower than those occurring in operating nuclear reactor cores. Compared to LES, URANS have much lower computer resource requirements than LES, and can handle flows at larger Reynolds numbers. Consequently, one may conclude that URANS are still an acceptable choice for rod bundle CFD analysis. One should be encouraged to use LES instead, but only when it is possible to satisfy the well-established criteria that make LES what they are. The use of the segregated hybrid model is helpful in this respect, as it reduces the minimum channel length required for the LES analysis. If the recent growth of computer capabilities continues, it is possible that LES will eventually become the method of choice for the nuclear industry, but this time has not yet arrived.

For a final note following the previous discussion, we will revisit the CT simulations. Although CT predicted the occurrence and maintenance of the gap vortex street in the rod-wall gap region, they overpredicted the Strouhal number and underpredicted the turbulent kinetic energy in the gap, compared to measurements. These predictions, however, were improved in the present simulations which used the same URANS model as CT, but considered a developing flow, rather than employing a streamwise-periodic boundary condition as CT did. This demonstrates that a poor prediction of the vortex street Strouhal number is not an inherent inadequacy of the URANS method, but is rather attributable to the use of the streamwise-periodic boundary condition. It appears that the channel length of 20D for the CT simulations was not long enough for the results to be independent of it. The choice for that computational length was dictated by the maximum computer power available to CT at the time and was, to some degree, justified by the spatial decorrelation of turbulent statistics over that distance in the GT experiment. The present results show that, had CT run developing flow simulations with a channel length of 20D, they would not have captured the onset of gap instability and might have concluded that URANS are unable to predict this phenomenon. Since the CT work, the continuing growth of computer power has made it possible to compute developing flows in long complex channels with the URANS method. Therefore, it seems no longer necessary to use the streamwise-periodic boundary condition for URANS simulations of rod-bundle flows.

5. Acknowledgments

Financial support was provided by the Natural Sciences and Engineering Research Council of Canada (NSERC) and the Atomic Energy of Canada Limited (AECL).

6. References

[1] G. Hofmann, "Qualitative investigation of local heat transfer coefficients in a 7-rod bundle", Report No. 13, Institüt für Reaktorbauelemente, Kernforschungzentrum Karlsruhe, Germany, June, 1964 (in German – unpublished).

[2] J.D. Hooper and K. Rehme, "Large-scale structural effects in developed turbulent flow through closely-spaced rod arrays", Journal of Fluid Mechanics, Vol. 145, 1984, pp. 305-337.

[3] S.V. Möller, "Single-phase turbulent mixing in rod bundles", Experimental Thermal and Fluid Science, Vol. 5, 1992, pp. 26-33.

[4] T. Krauss and L. Meyer, "Experimental investigation of turbulent transport of momentum and energy in a heated rod bundle", Nuclear Engineering and Design, Vol. 180, 1998, pp. 185-206.

[5] M.S. Guellouz and S. Tavoularis, "The structure of turbulent flow in a rectangular channel containing a cylindrical rod – Part1: Reynolds-averaged measurements", Experimental Thermal and Fluid Science, Vol. 23, 2000, pp. 59-73.

[6] M.S. Guellouz and S. Tavoularis, "The structure of turbulent flow in a rectangular channel containing a cylindrical rod – Part2: Phase-averaged measurements", Experimental Thermal and Fluid Science, Vol. 23, 2000, pp. 75-91.

[7] F. Baratto, S.C.C. Bailey, and S. Tavoularis, "Measurements of frequencies and spatial correlations of coherent structures in rod bundle flows", Nuclear Engineering and Design, Vol. 236, 2006, pp. 1830-1837.

[8] A.S. Lexmond, R.F. Mudde, and T.H.J.J. van der Hagen, "Visualization of the vortex street and characterization of the cross flow in the gap between two sub-channels", 11th International Topical Meeting on Nuclear Reactor Thermal Hydraulics (NURETH), Avignon, France, 2005.

[9] A. Mahmodd, M. Rohde, T.H.J.J. van der Hagen, and R.F. Mudde, "An experimental study of cross flow in a single phase between two channels connected by a near wall curved gap region", 7th International Topical Meeting on Nuclear Reactor Thermal Hydraulics, Operations and Safety (NUTHOS), Seoul, Korea, 2008.

[10] I. Khabbouchi, M.S. Guellouz, and S. Tavoularis, "Influence of coherent structures on the wall shear stress in axial flow between a cylinder and a plane wall", International Symposium on Convective Heat and Mass Transfer in Sustainable Energy (CONV-09), Hammamet, Tunisia, 2009 April 26-May 1.

[11] W.J. Seale, "Turbulent diffusion of heat between connected flow passages", Nuclear Engineering and Design, Vol. 54, 1979, pp. 197-209.

[12] C.W. Rapley and A.D. Gosman, "The prediction of fully developed axial turbulent flow in rod bundles", Nuclear Engineering and Design, Vol. 97, 1986, pp. 313-325.

[13] K.A. Antonopoulos, "The prediction of turbulent inclined flow in rod bundles", Computers & Fluids, Vol. 14, 1986, pp. 313-325.

[14] K.B. Lee and H.C. Jang, "A numerical prediction on the turbulent flow in closely spaced bare rod arrays by a nonlinear *k*-*ε* model", Nuclear Engineering and Design, Vol. 172, 1997, pp. 351-357.

[15] W.J. Seale, "Measurements and predictions of fully developed turbulent flow in a simulated rod bundle", Journal of Fluids Mechanics, Vol. 123, 1982, pp. 399-423.

[16] H.G. Kaiser and W. Zeggel, "Turbulent flows in complex rod bundle geometries numerically predicted by the use of FEM and a basic turbulence model", Nuclear Engineering and Design, Vol. 99, 1987, pp. 351-363.

[17] X. Wu, "Numerical study on the turbulence structures in closely spaced rod bundle subchannels", Numerical Heat Transfer, Part A, Vol. 25, 1994, pp. 649-670.

[18] S. Kim, and G.-C. Park, "Estimation of anisotropic factor and turbulent mixing rate in rod bundles based on the flow pulsation phenomenon", Nuclear Technology, Vol. 117, 1997, pp. 340-352.

[19] E. Baglietto and H. Ninokata, "A turbulence model study for simulating flow inside tight lattice rod bundle", Nuclear Engineering and Design, Vol. 235, 2005, pp. 773-784.

[20] S. Tavoularis, A. Madrane, and R. Vaillancourt, "Numerical simulation of coherent structures in axial flow through a rectangular channel containing a cylindrical rod" Proceedings of 10th Annual Conference of the CFD Society of Canada, Windsor, Ontario, Canada, 2002 June 9-11.

[21] D. Chang and S. Tavoularis, "Unsteady numerical simulations of turbulence and coherent structures in axial flow near a narrow gap", ASME Journal of Fluids Engineering, Vol. 127 No. 3, 2005, pp. 458-466.

[22] D. Chang and S. Tavoularis, "Convective heat transfer in turbulent flow near a gap", ASME Journal of Heat Transfer, Vol. 128, 2006, pp. 701-708.

[23] D. Chang and S. Tavoularis, "Numerical simulation of turbulent flow in a 37-rod bundle", Nuclear Engineering and Design, Vol. 237, 2007, pp. 575-590.

[24] D. Chang and S. Tavoularis, "Simulations of turbulence, heat transfer and mixing across narrow gaps between rod-bundle subchannels", Nuclear Engineering and Design, Vol. 238, 2008, pp. 109-123.

[25] D. Home, G. Arvanitis, M.F. Lightstone, and M.S. Hamed, "Simulation of flow pulsations in a twin rectangular sub-channel geometry using unsteady Reynolds averaged Navier-Stokes modelling", Nuclear Engineering and Design, Vol. 239, 2009, pp. 2964-2980.

[26] H. Ninokata, E. Merzari, and A. Khakim, "Analysis of low Reynolds number turbulent flow phenomena in nuclear fuel pin subassemblies of tight lattice configuration", Nuclear Engineering and Design, Vol. 239, 2009, pp. 855-866.

[27] B.H. Yan, H.Y. Gu, and L. Yu, "Unsteady Reynolds averaged Navier-Stokes simulation of the turbulent flow pulsation and coherent structures in a tight lattice in rolling motion", Annals of Nuclear Energy, Vol. 38, 2011, pp. 1023-1032.

[28] R.C.K. Rock and M.F. Lightstone, "A numerical investigation of turbulent interchange mixing of axial coolant flow in rod bundle geometries", Numerical Heat Transfer, Part A, Vol. 40, 2001, pp. 221-237.

[29] W.K. In, C.H. Shin, D.S. Oh, and T.H. Chun, "Assessment of the CFD analysis for the turbulent flow in fuel rod bundle" Proceedings of International Congress on Advances in Nuclear Power Plants (ICAPP), Seoul, Korea, 2005 May 15-19.

[30] C. Tzanos, "Computational fluid dynamics for the analysis of light water reactor flows", Nuclear Technology, Vol. 147, 1984, pp. 147-163.

[31] G. Házi, "On turbulence models for rod bundle flow computations", Annals of Nuclear Energy, Vol. 32, 2005, pp. 755-761.

[32] X. Cheng and N.I. Tak, "CFD analysis of thermal-hydraulic behaviour of heavy liquid metals in sub-channels", Nuclear Engineering and Design, Vol. 236, 2006, pp. 1874-1885.

[33] X. Cheng and Y.Q. Yu, "Local thermal-hydraulic behaviour in tight 7-rod bundles", Nuclear Engineering and Design, Vol. 239, 2009, pp. 1944-1955.

[34] M.E. Conner, E. Baglietto, and A. Elmahdi, "CFD methodology and validation for single-phase flow in PWR fuel assemblies", Nuclear Engineering and Design, Vol. 240, 2010, pp. 2088-2095.

[35] C.C. Liu and Y.M. Ferng, "Numerical simulating the thermal-hydraulic characteristics within the fuel rod bundle using CFD methodology", Nuclear Engineering and Design, Vol. 240, 2010, pp. 3078-3086.

[36] L. Chandra, F. Roelofs, M. Houkema, and B. Jonker, "A stepwise development and validation of a RANS based CFD modelling approach for the hydraulics and thermal-hydraulic analyse of liquid metal flow in a fuel assembly", Nuclear Engineering and Design, Vol. 239, 2009, pp. 1988-2033.

[37] S. Tóth and A. Aszódi, "CFD analysis of flow field in a triangular rod bundle", Nuclear Engineering and Design, Vol. 239, 2010, pp. 352-363.

[38] G. Yadigaroglu, M. Andreani, J. Dreier and P. Coddington, "Trends and needs in experimentation and numerical simulation for LWR safety", Nuclear Engineering and Design, Vol. 221, 2003, pp. 205-223.

[39] G. Mayer and G. Házi, "Direct numerical and large eddy simulation of longitudinal flow along triangular array of rods using the lattice Boltzmann method", Mathematics and Computers in Simulations, Vol. 72, 2006, pp. 173-178.

[40] G. Mayer, J. Páles, and G. Házi, "Large eddy simulation of subchannels using the lattice Boltzmann method", Annals of Nuclear Energy, Vol. 34, 2007, pp. 140-149.

[41] W. Wang and R. Pletcher, "Large eddy simulation of compressible flows in a rectangular duct containing cylindrical rods – an immersed boundary treatment", 45th AIAA Aerospace Sciences Meeting and Exhibit, AIAA 2007-921, Reno, USA, 2007.

[42] E. Merzari, H. Ninokata, and E. Baglietto, "Numerical simulation of flows in tight-lattice fuel bundles", Nuclear Engineering and Design, Vol. 238, 2008, pp. 1703-1719.

[43] F. Abbasian, S.D. Yu, and J. Cao, "Experimental and numerical investigations of three-dimensional turbulent flow of water surrounding a CANDU simulation fuel bundle structure inside a channel", Nuclear Engineering and Design, Vol. 239, 2009, pp. 2224-2235.

[44] F. Abbasian, S.D. Yu, and J. Cao, "Large eddy simulation of turbulent axial flow along an array of rods", Journal of Fluids Engineering, Vol. 132, 2010, p. 021105.

[45] T. Ikeno and T. Kajishima, "Analysis of dynamical flow structure in a square arrayed rod bundle", Nuclear Engineering and Design, Vol. 240, 2010, pp. 305-312.

[46] E. Baglietto, H. Ninokata, T. Misawa "CFD and DNS methodologies development for fuel bundle simulations", Nuclear Engineering and Design, Vol. 236, 2006, pp. 1503-1510.

[47] S. Tavoularis, "Rod bundle vortex networks, gap vortex streets, and gap instability: a nomenclature and some comments on available methodologies", Nuclear Engineering and Design, Vol. 241, 2011, pp. 2624-2626.

[48] A. Gosset and S. Tavoularis, "Laminar flow instability in a rectangular channel with a cylindrical core", Physics of Fluids, Vol. 18, 2006, p. 044108.

[49] E. Piot and S. Tavoularis, "Gap instability of laminar flows in eccentric annular channels", Nuclear Engineering and Design, 2011, in press.

[50] G.R. Tabor, M.H. Baba-Ahmadi, "Inlet conditions for large eddy simulation: a review", Computers & Fluids, Vol. 39, 2010, pp. 553-567.

[51] R.H. Kraichnan, "Diffusion by a random velocity field", Physics of Fluids, Vol. 13, 1970, pp. 22-31.

[52] R. Smirnov, S. Shi, and I. Celik, "Random flow generation technique for large eddy simulations and particle dynamics modelling", Journal of Fluids Engineering, Vol. 123, 2001, pp. 359-371.

[53] M.E. Sergent, "Vers une Méthodologie de Couplage Entre la Simulation des Grandes Echelles et les Modèles Statistiques", Phd Thesis, Ecole Cetnral de Lyon, 2002.

[54] F. Mathey, D. Cokljat, J.P. Bertoglio, and E. Sergent, "Specification of LES inlet boundary condition using vortex method", 4th International Symposium on Turbulence, Heat and Mass Transfer, Antalya, Turkey, 2003.

[55] N.J. Georgiadis, D.P. Rizzetta, C. Fureby, "Large-eddy simulation: current capabilities, recommended practices, and future research", 47th Aerospace Sciences Meeting, AIAA 2009-948, Orlando, USA, 2009.

[56] C.M. Rhie and W.L. Chow, "Numerical study of the turbulent flow past an airfoil with trailing edge separation", AIAA Journal, Vol. 21, 1983, pp. 1523-1532.

[57] J.P. Van Doormal and G.D. Raithby, "Enhancements of the SIMPLE method for predicting incompressible fluid flows", Numerical. Heat Transfer, Vol. 7, 1984, pp. 147-163.

[58] B.E. Launder, "Second-moment closure: present … and future?", International Journal of Heat and Fluid Flow, Vol. 9, 1989, pp. 963-985.

[59] B.E. Launder and N. Shima, "Second-moment closure for the near-wall sublayer: development and application", AIAA Journal, Vol. 27, No. 10, 1989, pp. 1319-1325.

[60] C.J. Chen and S.Y. Jaw, "Fundamentals of turbulence modelling", Taylor & Francis, Washington DC, USA, 1998.

[61] B.E. Launder, G.J. Reece, and W. Rodi, "Progress in development of a Reynolds-stress turbulence closure", Journal of Fluid Mechanics, Vol. 68, No. 3, 1975, pp. 537-566.

[62] D.C. Wilcox, "Turbulence modelling for CFD", DCW Industries, Inc., La Canada, California, USA 1998.

[63] F.R. Menter and Y. Egorov, "A scale-adaptive simulation model using two-equation models", 43th Aerospace Science Meeting and Exhibit, AIAA paper 2005-1095, Reno, NV, USA, 2005.

[64] D. Chapman, "Computational aerodynamics, development and outlook", AIAA Journal, Vol. 17, 1979, pp. 1293-1313.

[65] P.R., Spalart, W.-H. Jou, M. Strelets, and S.R. Allmars, "Comments on the feasibility of LES for wings, and on a hybrid RANS/LES approach", 1st AFOSR International Conference on DNS/LES, Ruston, LA, USA, 1997.

[66] M.L. Shur, P.R. Spalart, M.K. Strelets, and A.K. Travin, "A hybrid RANS-LES approach with delayed-DES and wall-modelled LES capabilities", International Journal of Heat and Fluid Flow, Vol. 29, No. 6, 2008, pp. 1638-1649.

[67] F. Mathey, "Aerodynamic noise simulation of the flow past an airfoil trailing-edge using a hybrid zonal RANS-LES", Computers & Fluids, Vol. 37, 2008, pp. 836-843.

[68] F. Nicoud and F. Ducros, "Subgrid-scale stress modelling based on the square of the velocity gradient tensor flow", Turbulence and Combustion, Vol. 62, No. 3, 1999, pp. 183–200.

[69] L. Bricteux, M. Duponcheel, and G. Wickelmans, "A multiscale subgrid model for both free vortex flows and wall-bounded flows", Physics of Fluids, Vol. 21, 2009, p. 105102.

[70] M. Weickert, G. Teike, O. Schmidt, and M. Sommerfeld, "Investigation of the LES WALE turbulence model within the lattice Boltzmann framework", Computers and Mathematics with Applications, Vol. 59, 2010, pp. 2200-2214.

[71] S. Wornom, H. Ouvrard, M. V. Salvetti, B. Koobus, and A. Dervieux, "Variational multiscale large-eddy simulations of the flow past a circular cylinder: Reynolds number effects", Computers & Fluids, Vol. 47, 2011, pp.44-50.

[72] B.H., Ouma and S. Tavoularis, "Turbulence structure in triangular subchannels of a reactor bundle model", Nuclear Engineering and Design, Vol. 128, 1991, pp. 271-287.

[73] B.H., Ouma and S. Tavoularis, "Flow measurements in a rod bundle subchannels with varying rod-wall proximity", Nuclear Engineering and Design, Vol. 131, 1991, pp. 193-208.